The Pristine Inner Galaxy Survey (PIGS) VII: a discovery of the first inner Galaxy CEMP-r/s star

L. Mashonkina, A. Arentsen, D. S. Aguado, A. Smogorzhevskii, M. Hampel, A. I. Karakas, F. Sestito, N. F. Martin, K. A. Venn, J. I. González Hernández

Monthly Notices of the ROYAL ASTRONOMICAL SOCIETY

MNRAS **523,** 2111–2125 (2023) https://doi.org/10.1093/mnras/stad1536
Advance Access publication 2023 May 19

The Pristine Inner Galaxy Survey (PIGS) VII: a discovery of the first inner Galaxy CEMP-r/s star

L. Mashonkina [1]★ A. Arentsen [2]★ D. S. Aguado,[3,4] A. Smogorzhevskii,[1,5] M. Hampel,[6] A. I. Karakas [6,7] F. Sestito [8] N. F. Martin [9,10] K. A. Venn [8] and J. I. González Hernández[3,4]

[1]*Institute of Astronomy of the Russian Academy of Sciences, Pyatnitskaya st. 48, 119017 Moscow, Russia*
[2]*Institute of Astronomy, University of Cambridge, Madingley Road, Cambridge CB3 0HA, UK*
[3]*Instituto de Astrofísica de Canarias, Vía Láctea, 38205 La Laguna, Tenerife, Spain*
[4]*Universidad de La Laguna, Departamento de Astrofísica, 38206 La Laguna, Tenerife, Spain*
[5]*M. V. Lomonosov Moscow State University, Kolmogorova st. 1, 119991 Moscow, Russia*
[6]*School of Physics and Astronomy, Monash University, Clayton, VIC 3800, Australia*
[7]*ARC Centre of Excellence for All Sky Astrophysics in 3 Dimensions (ASTRO 3D), Melbourne, VIC, Australia*
[8]*Department of Physics and Astronomy, University of Victoria, PO Box 3055, STN CSC, Victoria BC V8W 3P6, Canada*
[9]*Observatoire Astronomique de Strasbourg, Université de Strasbourg, CNRS, UMR 7550, F-67000 Strasbourg, France*
[10]*Max-Planck-Institut für Astronomie, Königstuhl 17, D-69117 Heidelberg, Germany*

Accepted 2023 May 17. Received 2023 May 4; in original form 2023 April 6

ABSTRACT

Well-studied very metal-poor (VMP, [Fe/H] <-2) stars in the inner Galaxy are few in number, and they are of special interest because they are expected to be among the oldest stars in the Milky Way. We present high-resolution spectroscopic follow-up of the carbon-enhanced metal-poor (CEMP) star Pristine_184237.56-260624.5 (hereafter Pr184237) identified in the Pristine Inner Galaxy Survey. This star has an apocentre of $\sim$2.6 kpc. Its atmospheric parameters ($T_{\rm eff}$ = 5100 K, $\log g$ = 2.0, and [Fe/H] = -2.60) were derived based on the non-local thermodynamic equilibrium (NLTE) line formation. We determined abundances for 32 elements, including 15 heavy elements beyond the iron group. The NLTE abundances were calculated for 13 elements from Na to Pb. Pr184237 is strongly enhanced in C, N, and O, and both s- and r-process elements from Ba to Pb; it reveals a low carbon isotope ratio of ^{12}C/^{13}C = 7. The element abundance pattern in the Na–Zn range is typical of halo stars. With [Ba/Eu] = 0.32, Pr184237 is the first star of the CEMP-r/s subclass identified in the inner Galaxy. Variations in radial velocity suggest binarity. We tested whether a pollution by the s- or i-process material produced in the more massive and evolved companion can form the observed abundance pattern and find that an i-process in the asymptotic giant branch star with a progenitor mass of 1.0–2.0 $M_\odot$ can be the solution.

Key words: stars: abundances – stars: atmospheres – galaxies: abundances.

1 INTRODUCTION

Studies of very metal-poor (VMP; [Fe/H][1] <-2.0) stellar populations in the Milky Way are important to understand the early Universe. Their detailed chemical abundances teach us about the properties of the First Stars and early star formation, and their chemo-dynamics shed light on the early formation history of our Galaxy (Frebel & Norris 2015). The central regions of our Galaxy ($\lesssim$ 5 kpc) are predicted to host the oldest metal-poor stars (Tumlinson 2010), which are important probes of the earliest metal-free stars in the Universe. In recent years, significant efforts have been made to build larger samples of VMP stars in the inner Galaxy (Howes et al. 2015, 2016; Lucey et al. 2019; Arentsen et al. 2020b) – a challenging endeavour because the overwhelming majority of bulge stars have high metallicity, and the high extinction and the relatively large distance from the Sun make clean selections of metal-poor stars difficult. These surveys typically employ narrow-band photometry to identify metal-poor stars, which has been very effective.

Recent studies show that VMP stars in the inner Galaxy appear to have similar abundances to stars in previous halo samples, although there are some subtle differences in, e.g. the scatter and correlations of various abundances (Howes et al. 2016; Koch et al. 2016; Lucey et al. 2019; Sestito et al. 2023). One other striking difference is an apparent lack of carbon-enhanced metal-poor (CEMP) stars (Howes et al. 2016; Arentsen et al. 2021), with the common definition for CEMP stars having [C/Fe] $>+0.7$ (Aoki et al. 2007). In the Galactic halo, many of the most metal-poor stars are found to be rich in carbon, representing 20 per cent and 43 per cent of stars with [Fe/H] ≤-2 and ≤-3, respectively (Placco et al. 2014). For the bulge, Arentsen et al. (2021) found a CEMP fraction of only 16 per cent for [Fe/H] <-2.5 in the low-resolution spectroscopic Pristine Inner Galaxy Survey (PIGS). They discuss that it might partly be related to selection effects against carbon-rich stars, but argue that it cannot be explained away entirely. The lower CEMP fraction could be due

★ E-mail: lima@inasan.ru (LM); anke.arentsen@ast.cam.ac.uk (AA)
[1]In the classical notation, where [X/Y] $= \log(N_{\rm X}/N_{\rm Y})_{star} - \log(N_{\rm X}/N_{\rm Y})_\odot$ for each pair of elements X and Y.

to a lower number of binary stars in the inner Galaxy, and/or due to faster and more intense early star formation – both scenarios would be indications that the metal-poor stellar populations in the inner Galaxy and the more distant halo formed in different environments.

Depending on abundances of the elements produced presumably in the slow (s) or rapid (r) neutron-capture processes, which can be derived from high-resolution spectroscopy, CEMP stars are separated into CEMP-r ([Eu/Fe] >1), CEMP-s ([Ba/Fe] >1, and [Ba/Eu] >0.5), CEMP-r/s (enhanced in both barium and europium with 0 < [Ba/Eu] <0.5), and CEMP-no ([Ba/Fe] <0) stars, as suggested by Beers & Christlieb (2005). Slightly different numbers are recommended by Abate, Stancliffe & Liu (2016) and Frebel (2018) to characterize different groups. Being purely phenomenological, this separation turns out to be indicative of the nature of stars in different groups. Excess of carbon and s-process elements in a CEMP-s star is thought to be the result of mass transfer from an asymptotic giant branch (AGB) star to a companion in a binary system. This hypothesis is supported by radial velocity variations observed for many CEMP-s stars (Hansen et al. 2016). The CEMP-no stars, which are typically not in binary systems, likely formed out of the interstellar matter enriched by the Population III stars, which either were rapidly rotating (Chiappini et al. 2006) or exploded as faint supernovae (Nomoto, Kobayashi & Tominaga 2013, and references therein). CEMP-r stars are similar to CEMP-no stars, except that they are enhanced in r-process elements, which they were likely born with as well. The nature of CEMP-r/s stars is under debate, and various scenarios of enrichment in heavy elements are considered, from mass transfer in a binary system formed out of the interstellar matter rich in the r-process elements to the operation of the intermediate neutron-capture process (i-process, see Goswami, Rathour & Goswami 2021, for a review).

Detailed studies of CEMP stars can provide a unique information about the early chemical enrichment of the inner Galaxy, but they are only available in the literature for a very few stars. Four CEMP-no stars, all with [Fe/H] <−3 and low Ba abundances, were discovered in the EMBLA (Extremely Metal-poor BuLge stars with AAOmega) sample (Howes et al. 2015, 2016): one was reported by Howes et al. (2015), and three additional stars were found by Arentsen et al. (2021) when applying the evolutionary carbon corrections from Placco et al. (2014). The three CEMP stars with close together metallicities of [Fe/H] $\simeq$ −2.5 were found to be strongly enhanced in Ba, with [Ba/Fe] >+1. One of them was classified by Koch et al. (2016) as CEMP-s based on low upper limits for abundances of the r-process elements Eu and Dy. None of the r-process elements were measured by Sestito et al. (2023) in the remaining two CEMP stars, due to a limited wavelength range of their Gemini GRACES spectra.

In this work, we report the detailed analysis of a new CEMP star in the inner Galaxy, Pristine_184237.56-260624.5 (for short, Pr184237), with [Fe/H] = −2.6 and [C/Fe] = +1.8, which is enhanced in both s- and r-process elements. It was observed as part of a high-resolution spectroscopic follow-up campaign of the most metal-poor stars in PIGS, undertaken with UVES[2] at the VLT. It deserved a careful, dedicated analysis due to the high carbon and neutron-capture element abundances, which we report on here separately from the main sample. We performed a detailed line-by-line analysis of the spectrum of Pr184237 in a wide wavelength range and determined abundances for 32 chemical elements, including 15 neutron-capture elements. Abundances for 13 chemical elements are based on the non-local thermodynamic equilibrium (NLTE) line formation, which is important because the physical conditions in atmospheres of VMP giants are favourable for the departures from local thermodynamic equilibrium (LTE).

The paper is organized as follows. We introduce PIGS and the high-resolution observations of Pr184237 in Section 2. Section 3 describes the NLTE methods and codes used. Section 4 discusses the determination of the star's atmospheric parameters. Elemental abundances are derived in Section 5, and Section 6 discusses the possible origins of the heavy element abundance pattern of Pr184237. Our conclusions are given in Section 7.

2 OBSERVATIONS OF PR184237

The PIGS, an extension of the main Pristine survey (see Starkenburg et al. 2017, for an overview), was initiated to build an unprecedentedly large sample of metal-poor and VMP stars for chemo-dynamical studies of the inner regions of the Galaxy (Arentsen et al. 2020a,b, 2021). Using metallicity-sensitive *CaHK* photometry from the Canada–France–Hawaii-Telescope (CFHT), PIGS selects metal-poor candidates for spectroscopic follow-up. The next step is an intermediate-resolution spectroscopy with the AAOmega spectrograph (Saunders et al. 2004) on the Anglo-Australian Telescope combined with determinations of the stellar atmosphere parameters using the ULySS (Koleva et al. 2009) and FERRE (Allende Prieto et al. 2006) tools. A total of 1900 VMP stars were identified in the PIGS-AAT sample. Aiming to understand the nucleosynthesis processes in the ancient inner Galaxy, ∼20 of the most metal-poor stars were selected from the AAT sample for high-resolution spectroscopy with the UVES/VLT, one of which was Pr184237.

Pr184237 was found to have [Fe/H] = −2.8 and [C/Fe] = +2.0 from the low-resolution spectroscopy and was recognized as a CEMP star in Arentsen et al. (2021). The AAT barycentric radial velocity is -12.5 ± 2.0 km s^{-1}. It is located at (RA, Dec) = (18:42:37.56,−26:06:24.5) and (l, b) = (8.514105°, −9.783936°) and identified with Gaia DR3 source_id 4073253907337129472 of G magnitude = 15.52 (Gaia Collaboration et al. 2022). It has E(B-V) = 0.38 (Green et al. 2019).

2.1 UVES observations

The UVES observations of Pr184237 were originally scheduled for period 105 in queue mode. However, due to COVID restrictions in Paranal (Chile), observations were taken in period 107. The employed setup was #*Dic*1 (390 + 580) with a 1.″2 slit, 1 × 1 binning and low readout speed. This configuration led to a resolving power of $R \sim 45\,000$ in the blue part of the spectrum (330−452 nm) and $R \sim 41\,500$ for the red (480−680 nm). Three observations were taken between the third and the fourth of June 2021 with an exposure time of 3000 s each and an average signal-to-noise ratio (SNR) of 7 and 32 at 380 nm and 510 nm, respectively.

The data were reduced by the ESO pipeline and retrieved by a query on the phase 3 online interface.[3] The barycentric correction was applied with IRAF and the radial velocity was calculated with a cross-correlation function to a UVES template with the `fxcor` package, after which the three spectra were combined in the rest frame with a 'sigclip' algorithm. The three radial velocities are reported in Table 1, together with the AAT radial velocity.

[2]Ultraviolet and visual Echelle spectrograph.

[3]https://www.eso.org/sci/observing/phase3.html

Table 1. Radial velocities of Pr184237.

Instrument	MJD (days)	RV ($km\,s^{-1}$)
AAT	58337.44	-12.5 ± 2.0
UVES	59368.37	-39.3 ± 1.0
UVES	59369.33	-39.1 ± 1.0
UVES	59369.36	-39.8 ± 1.0

A first full-spectrum fitting analysis of the UVES spectrum was performed with the FERRE[4] code following the same procedure explained in Aguado et al. (2021a,b). In brief, the code is able to fit the data and interpolate between the nodes of a grid of stellar models computed with ASSET (Koesterke, Allende Prieto & Lambert 2008) and ATLAS (Sbordone 2005) codes of spectral synthesis. These models already contain carbon-enrichment, an important feature when analyzing metal-poor stars (see e.g. Aguado et al. 2017, for more information about the carbon models). The four parameters FERRE derived for Pr184237 are effective temperature ($T_{\rm eff}$ = 5448 ± 123 K), surface gravity ($\log g$ = 2.01 ± 0.26), overall metallicity ([Fe/H] = −2.46 ± 0.10), and carbon enrichment ([C/Fe] = 2.19 ± 0.12). A preliminary automatic abundance analysis with FERRE indicated that Pr184237 is enhanced in both s-process ([Ba/Fe] = 1.04, [La/Fe] = 0.56) and r-process ([Eu/Fe] = 0.6) elements, suggesting that this is the first CEMP-r/s star in the inner Galaxy. This encouraged us to do a dedicated detailed analysis (see Sections 4 and 5). The FERRE analysis for the full PIGS-UVES sample will be presented in a forthcoming paper (Aguado et al., in preparation).

2.2 Variability and binarity

The AAT baricentric radial velocity ($-12.5 \pm 2.0\ km\,s^{-1}$) is significantly different from the three UVES radial velocities taken almost 3 yr later ($-39.4\ km\,s^{-1}$ with a standard deviation of $0.3\ km\,s^{-1}$). The precision of the AAT radial velocities was estimated by Arentsen et al. (2020b) to be around $2\ km\,s^{-1}$. A more recent comparison with Gaia DR3 radial velocities for the full AAT sample (where available, only for brighter stars and not for Pr184237) shows that the uncertainty estimate was correct and possibly even slightly overestimated (Arentsen et al. in preparation). Therefore the difference between the AAT and UVES radial velocities can be taken as a clear indication that this star is in a binary (or multiple) system.

We also found that Pr184237 was flagged as a photometrically variable star in Gaia DR3, with the classification 'ELL' (Rimoldini et al. 2022, best class score = 0.58) – an ellipsoidal variable, which is a close binary system where the stars are deforming and projection effects during the orbit cause photometric variability. There is a Gaia light curve available for this star, with variations on the order of ∼0.03 mag on a short time-scale (less than a few days). Fitting the epoch photometry with LIGHTKURVE (Lightkurve Collaboration et al. 2018) we found a best period of 1.8 d, but it was not very significant. Such a short period (if this star really was an ellipsoidal variable in a binary system) is not consistent with our UVES observations. The UVES radial velocities taken over 2 d do not show any significant radial velocity variation, and there is also no sign of severe rotational line broadening. One could maybe imagine a scenario where this star is in a triple system, orbiting in a longer period around an inner short-period binary. In this scenario, the short-term variability could come from the inner binary. If the close binary consists of two white dwarfs, they should be too faint to contribute to the photometric variability since a white dwarf is ∼10 mag fainter than an RGB star like Pr184237 [related to the rapidly accreting white dwarf (RAWD) scenario discussed in Section 6.2].

However, inspecting images of Pr184237, we found that there is a faint star (∼4 mag fainter, G = 19.9) within ∼2″ of the main target. It has different proper motions so is not associated with Pr184237, but it might affect the photometry. We checked the Gaia scanning law and found that, for the epochs where Pr184237 appears brighter, Gaia scanned the sky exactly in the direction in which the two stars are aligned, and, when Pr184237 appears fainter, it was scanned perpendicular to that axis. The difference in flux between the two stars is similar to the amplitude of the photometric variability. Combined with the lack of evidence for a short orbital period from our UVES observations, we therefore concluded that the Gaia photometric variability is most likely spurious and not related to Pr184237 itself.

2.3 Orbit in the Milky Way

Stars that are currently in the inner Galaxy do not necessarily stay in the inner Galaxy – they could be outer halo stars just moving through. To test this for Pr184237, we derived its distance and orbital properties. The distance and orbits were derived adopting the same methodology used by Sestito et al. (2023) for the PIGS follow-up with the GRACES high-resolution spectrograph. Briefly, the Bayesian distance derivation uses the Gaia DR3 parallax and its uncertainty plus a prior on the stellar density distribution containing a disc and a halo (see Sestito et al. 2019 for more details about the method). For Pr184237, it resulted in a median distance of 7.97 ± 2.57 kpc (corresponding to a distance from the Galactic centre $d_{\rm GC} \approx 1.8$ kpc). The orbital integration is performed with GALPY (Bovy 2015) with the inclusion of a rotating bar in the gravitational potential. Then the orbital parameters are calculated from the distance probability distribution function. More details can be found in Sestito et al. (2023). We adopt a radial velocity of $-26.0\ km\,s^{-1}$, the average between the AAT and the UVES epochs, with an inflated uncertainty of $10\ km\,s^{-1}$ to represent that we do not actually know the systemic velocity. Adopting the above distance and radial velocity with their uncertainties and combining it with the Gaia DR3 proper motions, we derive the orbital properties of Pr184237, and find it has a median apocentre of 2.56 ± 0.93 kpc with a pericentre less than 1 kpc – it appears to be a real inner Galaxy star and not just a halo star passing through. Given that it is so tightly confined, the star is most likely to be of a 'proto-Galactic' origin (Belokurov & Kravtsov 2022; Rix et al. 2022) rather than accreted from a dwarf galaxy, or if it was accreted, this must have happened very early on.

3 ANALYSIS METHOD

We determined the NLTE abundances for Na, Mg, Al, Si, Ca, Sc, Ti, Fe, Zn, Sr, Ba, Eu, and Pb. Hereafter, these elements are referred to as NLTE species. For individual lines of Ti II, Fe I, and Zn I, the NLTE abundances were computed by adding the NLTE abundance corrections, $\Delta_{\rm NLTE} = \log \varepsilon_{\rm NLTE} - \log \varepsilon_{\rm LTE}$, to the LTE abundances. The $\Delta_{\rm NLTE}$ grids and interpolation tools are provided by Mashonkina, Sitnova & Pakhomov (2016b, Ti II, Fe I) and Sitnova et al. (2022, Zn I). For the remaining NLTE species, we performed the NLTE calculations using individual atmospheric parameters and elemental abundances of Pr184237 and the NLTE methods developed in our previous studies for Na I (Alexeeva, Pakhomov & Mashonkina 2014),

[4] http://github.com/callendeprieto/ferre

Mg I (Mashonkina 2013), Al I (Mashonkina, Belyaev & Shi 2016a), Si I–Si II (Mashonkina 2020), Ca I–Ca II (Mashonkina, Sitnova & Belyaev 2017b), Sc II (Mashonkina & Romanovskaya 2022), Sr II (Mashonkina et al. 2022), Ba II (Mashonkina & Belyaev 2019), Eu II (Mashonkina & Gehren 2000), and Pb I (Mashonkina, Ryabtsev & Frebel 2012).

The coupled radiative transfer and statistical equilibrium (SE) equations were solved with the code DETAIL (Giddings 1981; Butler 1984), where the background opacity was updated as described by Mashonkina et al. (2011). The computed departure coefficients, $b_i = n_i^{\rm NLTE}/n_i^{\rm LTE}$, were then used by the code SYNTHV_NLTE (Tsymbal, Ryabchikova & Sitnova 2019) to calculate the NLTE line profiles for a given NLTE species. Here, $n_i^{\rm NLTE}$ and $n_i^{\rm LTE}$ are the SE and thermal (Saha–Boltzmann) number densities, respectively.

The LTE and NLTE abundances were derived from line profile fitting using the code SYNTHV_NLTE (Tsymbal et al. 2019). The best fit to the observed spectrum is obtained automatically using the IDL BINMAG code by Kochukhov (2018). The line list required for calculations of the synthetic spectra, together with atomic data, were taken from the most recent version of Vienna Atomic Line Database (VALD; Ryabchikova et al. 2015) that includes isotopic splitting (IS) and hyper-fine splitting (HFS) components where they are available (Pakhomov, Ryabchikova & Piskunov 2019). The lines of the NLTE species were computed by implementing the departure coefficients from DETAIL, while LTE was assumed for the lines of the other species.

We used the homogeneous spherical model atmospheres with standard abundances (Gustafsson et al. 2008) from the MARCS website.[5] They were interpolated at the given effective temperature ($T_{\rm eff}$), surface gravity ($\log g$), and metallicity ([Fe/H]), applying the interpolation routine written by Thomas Masseron and available on the same website.

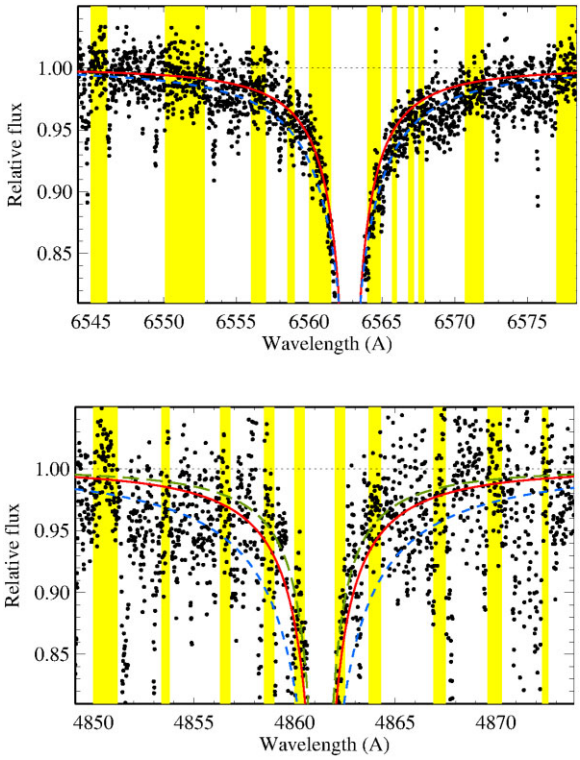

Figure 1. H_α (top panel) and H_β (bottom panel) line profiles in Pr184237 (bold dots) compared with the theoretical 3D-NLTE profiles from Amarsi et al. (2018) for $T_{\rm eff} = 5100$ K (red continuous curve), $T_{\rm eff} = 5450$ K (blue dashed curve), and $T_{\rm eff} = 4900$ K (green long-dashed curve, for H_β only). Everywhere, $\log g = 2.0$ and [Fe/H] $= -2.5$. The yellow shaded regions show the spectral windows used for the fit.

4 ATMOSPHERIC PARAMETERS

For Pr184237, the preliminary automatic FERRE analysis (Aguado et al., in preparation) yielded $T_{\rm eff} = 5450 \pm 123$ K, $\log g = 2.01 \pm 0.26$, and [Fe/H] $= -2.46 \pm 0.10$. In view of the extreme importance of derived elemental abundances for understanding the phenomenon of a CEMP-r/s star and for learning mechanisms of the early chemical enrichment of the inner Galaxy, we double checked and improved the atmospheric parameters of this star.

The effective temperature is derived by fitting the theoretical profiles computed by Amarsi et al. (2018) with three-dimensional (3D) hydrodynamic model atmospheres and based on the NLTE line formation to the observed wavelength regions free of blending lines in the wings of the Balmer H_α and H_β lines (Fig. 1). For both lines, the theoretical profiles corresponding to $T_{\rm eff} = 5450$ K are apparently deeper compared with the observed ones. Using a χ^2 minimization, we find that the best fit to H_α is achieved with $T_{\rm eff} = 5100$ K ($\chi^2 = 0.127$). For H_β, equal preference can be given to $T_{\rm eff} = 5100$ K and 4900 K due to similar $\chi^2 \simeq 0.4$. We give the greater weight to $T_{\rm eff}$ from H_α because of less important blending effects and higher S/N, and adopt $T_{\rm eff} = 5100$ K as our final effective temperature. From a comparison of the results from two lines, we estimate the uncertainty in $T_{\rm eff}$ as 100 K.

The surface gravity is constrained from a requirement of equal NLTE abundances determined from lines of the two ionization stages, Fe I and Fe II. We use the Fe I and Fe II lines and their atomic parameters, carefully selected and checked in our previous studies of VMP stars (Mashonkina et al. 2017a). In brief, for Fe I, we use presumably experimental *gf*-values, as listed by VALD, while, for Fe II, we apply *gf*-values from Raassen & Uylings (1998) that were corrected by +0.11 dex, following the recommendation of Grevesse & Sauval (1999). The exceptions are Fe II 4923 and 5018 Å, for which *gf*-values were obtained by averaging the data from the four sources – Bridges (1973); Moity (1983), Raassen & Uylings (1998), and Meléndez & Barbuy (2009). The van der Waals damping constants were taken from VALD.

We checked the surface gravity $\log g = 2.0$, which is very close to the FERRE value. The LTE and NLTE abundances are determined from lines of Fe I and Fe II using the model atmosphere with $T_{\rm eff}/\log g/$[Fe/H] $= 5100/2.0/-2.5$ and a microturbulent velocity of $\xi_t = 2$ km s^{-1}, which was calculated with the empirical formula deduced by Mashonkina et al. (2017a) for metal-poor Galactic halo giants. It provides an accuracy of 0.2 km s^{-1}. The results for individual lines are presented in Table 2. The mean Fe I- and Fe II-based NLTE abundances are found to be consistent within 0.02 dex: $\log \varepsilon_{\rm FeI} = 4.86 \pm 0.14$ (49 lines) and $\log \varepsilon_{\rm FeII} = 4.84 \pm 0.12$ (9 lines), while a difference in the LTE abundances amounts to −0.12 dex. Hereafter, we employ the abundance scale where $\log \varepsilon_{\rm H} = 12$. The abundance error is calculated as the dispersion in the single line measurements around the mean, $\sigma = \sqrt{\Sigma(\overline{x} - x_i)^2/(N_l - 1)}$. Here, N_l is the number of lines used. Taking into account that two independent methods provide consistent results, we estimate the uncertainty in $\log g$ as 0.1. Shifts of + 0.1/−0.1 in $\log g$ result in $\log \varepsilon_{\rm FeI} - \log \varepsilon_{\rm FeII} = -0.02/+0.06$ dex. Fig. 2 shows no trend of

[5] https://marcs.astro.uu.se

Table 2. Line atomic data, LTE, and NLTE abundances, log ε, for individual lines in Pr184237.

Species	λ (Å)	E_{exc} (eV)	log *gf*	LTE	NLTE
^{12}CH	4210.94	0.46	−1.34	7.49[1]	
^{12}CH	4210.99	0.46	−1.32	7.49[1]	
^{13}CH	4211.44	0.46	−1.34	7.49[1]	
^{13}CH	4211.49	0.46	−1.32	7.49[1]	
O I	6300.30	0.00	−9.94	7.45	
Na I	5889.95	0.00	0.12	≤3.94	≤3.37
Mg I	5528.41	4.33	−0.50	5.36	5.40

Notes. [1] For the ^{12}C/^{13}C = 7 isotope ratio. This table is available in its entirety in a machine-readable form in the online journal. A portion is shown here for guidance regarding its form and content.

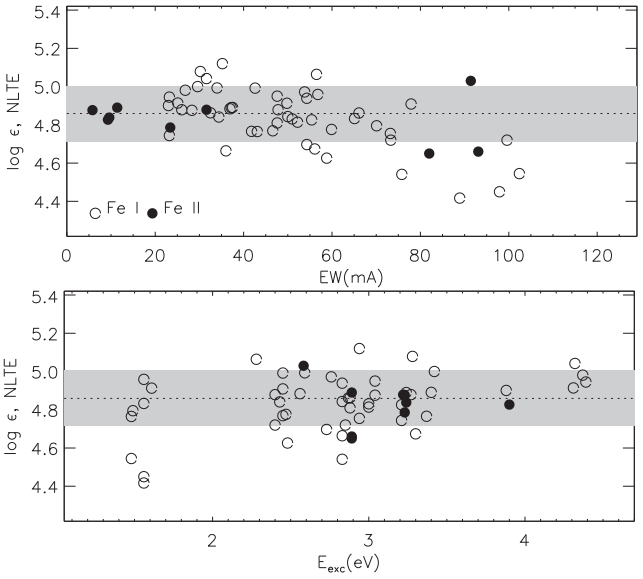

Figure 2. NLTE abundances from individual lines of Fe I (open circles) and Fe II (filled circles) in Pr184237 as a function of equivalent width EW (top panel) and excitation energy of the lower level (bottom panel). The dotted line indicates the mean Fe I-based abundance and the shaded grey area its statistical error.

the NLTE abundances with equivalent width, although there are four outliers that reveal a lower abundance compared with the mean, by more than 0.25 dex. The final Fe abundance is computed as the mean of $\varepsilon_{\rm FeI}$ and $\varepsilon_{\rm FeII}$.

Despite large reddening for the star observed towards the bulge, we have attempted to derive the effective temperature of our target from the infrared flux method (IRFM) of González Hernández & Bonifacio (2009), and that attempt was successful. We used the available photometry in the infrared bands from the Two Micron All-Sky Survey (2MASS, Skrutskie et al. 2006). The 2MASS JHK$_s$ magnitudes are accurate with J = 13.665 ± 0.024, H = 13.114 ± 0.027, and K$_s$ = 12.984 ± 0.030. We estimated the Johnson V magnitude (V = 15.942) ±0.012 converted from the Sloan PanSTARRS magnitudes g = 16.370 ± 0.003 and r = 15.550 ± 0.001 using equation (6) and coefficients from table 6 in Tonry et al. (2012). Magnitudes were de-reddened using E(B-V) = 0.38 (Green et al. 2019). The same reddening value of E(B-V)$_{\rm SFD}$ = 0.373 was computed from the dust maps of Schlegel, Finkbeiner & Davis (1998, SFD). Finally, E(B-V)$_{\rm SFD}$ was multiplied by a factor of 0.86 following Schlafly & Finkbeiner (2011). With E(B-V) = 0.321, we obtain $T_{\rm eff}$(IRFM) = 4999 ± 102, 5116 ± 67, and 5080 ± 86 K for the 2MASS bands J, H, and K$_s$, respectively. The IRFM-based mean temperature of Pr184237, $T_{\rm eff}$(IRFM) = 5073 ± 83 K, is consistent with that from the H$_\alpha$ wings. These calculations were performed with log g = 2 and [Fe/H] = −2.5.

Table 3. Determined stellar parameters of Pr184237.

Parameter	Value	Uncertainty
$T_{\rm eff}$	5100 K	± 100 K
log g	2.0	± 0.1
[Fe/H]	−2.60	± 0.14
ξ_t	2.0 km s^{-1}	± 0.2 km s^{-1}

We also inferred the effective temperature and surface gravity as in Sestito et al. (2023). Briefly, they develop a Monte Carlo method that consists in deriving the effective temperature using the Gaia photometry–temperature relation from Mucciarelli, Bellazzini & Massari (2021) and the surface gravity from the Stephan–Boltzmann equation. This method has been tested to provide compatible stellar parameters with spectroscopic inferences (e.g. Lardo et al. 2021; Sestito et al. 2023). We find a photometric $T_{\rm eff}$ = 5190 ± 100 K and log g = 2.25 ± 0.16. The spectroscopic and photometric temperatures agree within 0.63σ and the distance-based surface gravity for such a distant object and the spectroscopic one are compatible within 1.32σ.

Thus, we adopt $T_{\rm eff}$ = 5100 ± 100 K, log g = 2.0 ± 0.1, [Fe/H] = −2.60 ± 0.14, ξ_t = 2 ± 0.2 km s^{-1} as the final atmospheric parameters of Pr184237 (Table 3). In order to compute the metallicity, we use the solar Fe abundance log $\varepsilon_\odot$ = 7.45 from Lodders (2021).

5 CHEMICAL ABUNDANCES

The strongest lithium line, Li I 6707 Å, cannot be extracted from noise in the spectrum of Pr184237, suggesting a low Li abundance, as expected for a red giant (Iben 1967). In addition to iron, we are able to determine abundances for 31 chemical elements. Spectral lines for abundance analysis, together with their atomic data, are selected from the list provided by Mashonkina et al. (2010) for an r-process enhanced star, HE 2327-5642, with similar atmospheric parameters. For lines of Sc II, Mn I, Co I, Sr II, Ba II, La II, Eu II, and Yb II, the HFS and/or IS structure were properly taken into account.

The LTE and NLTE abundances obtained from individual lines are presented in Table 2. Table 4 lists the elemental average abundances together with their stochastic errors. Stochastic errors are caused by random uncertainties in the continuum placement, line profile fitting, and *gf*-values. They are represented by the dispersion in the measurements σ when $N_l > 1$. When only a single line or a molecular band is measured, the abundance error resembles the fit uncertainty provided by MPFIT (Markwardt 2009) and computed as $PERROR \cdot \sqrt{\chi^2/N_{DOF}}$, where N_{DOF} is the number of fitting degrees of freedom and *PERROR* is a formal parameter uncertainty, computed from the covariance matrix. In order to compute the abundance ratios relative to iron, [X/Fe], we used the present Solar system abundances recommended by Lodders (2021) and [Fe/H] = −2.60. For Na, Mg, Al, Si, Ca, Sc, Ti, and Zn, the [X/Fe] ratios are based on the NLTE abundances. For Cr, Mn, Co, and Ni, Table 4 indicates the LTE abundance ratio [X/Fe I], which is free, in part, from the departures from LTE. Since the NLTE abundances were determined for 4 of 15 heavy elements, the [X/Fe] ratios for all the heavy elements in Table 4 and the heavy element abundance pattern

Table 4. Elemental abundances of Pr184237.

Species	$\log \varepsilon_\odot$	$\log \varepsilon$		N_l	[X/Fe]
		LTE	NLTE		
C(C_2)	8.47	7.64(0.03)		1	1.77
N(CN)	7.85	6.54(0.10)		1	1.29
O I	8.73	7.45(0.03)		1	1.32
Na I	6.27	< 3.94	< 3.37	2	$<-0.30^{N}$
Mg I	7.52	5.36(0.02)	5.40(0.02)	1	0.48^{N}
Al I	6.42	3.31(0.15)	3.76(0.15)	1	-0.06^{N}
Si I	7.51	5.30(0.10)	5.27(0.10)	1	0.36^{N}
Ca I	6.27	4.04(0.11)	4.14(0.11)	7	0.47^{N}
Sc II	3.04	0.90(0.05)	0.90(0.05)	1	0.46^{N}
Ti II	4.90	2.72(0.12)	2.72(0.12)	9	0.42^{N}
V II	3.95	1.28(0.05)		2	−0.08
Cr I	5.63	2.81(0.06)		3	-0.09^{I}
Mn I	5.47	2.41(0.10)		1	-0.33^{I}
Fe I	7.45	4.72(0.13)	4.86(0.14)	49	0.01^{N}
Fe II	7.45	4.84(0.12)	4.84(0.12)	9	-0.01^{N}
Co I	4.86	2.44(0.05)		3	0.31^{I}
Ni I	6.20	3.40(0.18)		5	-0.07^{I}
Zn I	4.61	2.05(0.10)	2.22(0.10)	1	0.21^{N}
Sr II	2.88	0.27(0.05)	0.22(0.05)	2	−0.02
Y II	2.15	−0.24(0.20)		8	0.21
Zr II	2.55	0.67(0.22)		4	0.72
Ba II	2.17	0.74(0.08)	0.40(0.10)	3	1.17
La II	1.17	−0.33(0.13)		7	1.10
Ce II	1.58	0.09(0.19)		5	1.11
Nd II	1.45	−0.08(0.14)		10	1.07
Sm II	0.94	−0.55(0.13)		2	1.11
Eu II	0.51	−1.24(0.06)	−1.09(0.06)	4	0.85
Gd II	1.05	−0.77(0.08)		2	0.78
Dy II	1.12	−0.47(0.09)		5	1.01
Er II	0.92	−0.67(0.07)		3	1.01
Tm II	0.11	−1.00(0.05)		1	1.49
Yb II	0.91	−0.66(0.32)		1	1.03
Pb I	2.03	1.55(0.16)	2.21(0.16)	2	2.12

Note. The numbers in parentheses are the abundance errors. ^{N} Based on the NLTE abundance. ^{I} LTE abundance ratio [X/Fe I].

in our further analysis (Sections 5.4 and 6) are based on the LTE abundances, for consistency. In Section 6.3, we discuss the influence of using the NLTE abundances on our analysis of the nucleosynthesis scenarios.

We examined the systematic uncertainties in the derived elemental abundances of Pr184237, which are linked to the adopted stellar parameters. These were estimated by varying $T_{\rm eff}$ by 100 K, $\log g$ by 0.1, and ξ_t by -0.2 km s^{-1} in the model atmosphere. Table 5 summarizes the various sources of uncertainties. The total impact of varying $T_{\rm eff}$, $\log g$, and ξ_t is computed as the quadratic sum of Cols. 2–4 and denoted $\Delta(T, g, \text{and } \xi_t)$. Column 6 lists the stochastic errors $\sigma_{\rm obs}$, as given in Table 4. The total uncertainty $\sigma_{\rm tot}$ in the absolute abundance of each element is computed by the quadratic sum of the stochastic and systematic (Col. 5) errors.

The results for different groups of elements are described below.

5.1 Light elements C, N, O, and isotope ratio ^{12}C/^{13}C

The FERRE analysis discovered a strong enhancement of Pr184237 in carbon. In this study, we use a pronounced C_2 Swan band (5150–5170 Å) and determine the C abundance with an uncertainty of 0.03 dex. We confirm the FERRE conclusion although obtain the lower [C/Fe] = 1.77 due to adopting the lower effective temperature.

Table 5. Error budget for elemental abundances in Pr184237.

El.	ΔT 100 K	$\Delta \log g$ 0.1	$\Delta \xi_t$ −0.2 km s^{-1}	Δ (T, g, ξ_t)	$\sigma_{\rm obs}$	$\sigma_{\rm tot}$
(1)	(2)	(3)	(4)	(5)	(6)	(7)
C_2	0.14	−0.02	<0.01	0.14	0.03	0.14
CN	0.17	−0.02	<0.01	0.17	0.10	0.20
O I	0.07	0.03	<0.01	0.08	0.03	0.08
Mg I	0.06	<0.01	0.03	0.07	0.02	0.07
Al I	0.11	<0.01	0.10	0.15	0.15	0.21
Si I	0.11	<0.01	0.05	0.12	0.10	0.16
Ca I	0.07	<0.01	0.03	0.08	0.11	0.13
Sc II	0.05	0.04	0.02	0.07	0.05	0.08
Ti II	0.05	0.04	0.02	0.07	0.12	0.14
V II	0.05	0.04	0.01	0.06	0.05	0.08
Cr I	0.11	<0.01	0.02	0.11	0.06	0.13
Mn I	0.11	<0.01	0.05	0.12	0.10	0.16
Fe I	0.11	<0.01	0.05	0.12	0.13	0.18
Fe II	0.02	0.04	0.04	0.06	0.12	0.13
Co I	0.11	<0.01	<0.01	0.11	0.05	0.12
Ni I	0.11	<0.01	0.04	0.12	0.18	0.21
Zn I	0.07	0.01	<0.01	0.07	0.10	0.12
Sr II	0.09	0.01	0.11	0.14	0.05	0.15
Y II	0.06	0.03	0.03	0.07	0.20	0.21
Zr II	0.07	0.03	0.03	0.08	0.22	0.23
Ba II	0.09	0.03	0.14	0.17	0.08	0.19
La II	0.09	0.03	<0.01	0.09	0.13	0.16
Ce II	0.09	0.03	<0.01	0.09	0.19	0.21
Nd II	0.09	0.03	0.01	0.10	0.14	0.17
Sm II	0.09	0.03	<0.01	0.09	0.13	0.16
Eu II	0.09	0.03	<0.01	0.09	0.06	0.11
Gd II	0.09	0.03	<0.01	0.09	0.08	0.12
Dy II	0.09	0.03	0.01	0.10	0.09	0.13
Er II	0.09	0.03	<0.01	0.09	0.07	0.12
Tm II	0.09	0.03	<0.01	0.09	0.05	0.11
Yb II	0.06	0.03	0.09	0.11	0.32	0.34
Pb I	0.11	<0.01	0.02	0.11	0.16	0.20

New results are measurements for the N and O abundances. With fixed C abundance, the N abundance was determined from the CN band in the 4214–4216 Å region. For oxygen, we use the [O I] 6300 Å forbidden line, which is clearly detected in the spectrum of Pr184237. The star is found to be strongly enhanced in N and O, with [N/Fe] = 1.29 and [O/Fe] = 1.32.

Owing to the high carbon abundance, we derive the ^{12}C/^{13}C isotope abundance ratio from pairs of ^{12}CH 4210.9 Å and ^{13}CH 4211.4 Å molecular lines (Fig. 3). The calculations are performed with the solar mixture of C isotopes, ^{12}C/^{13}C = 95 (Lodders 2021), and with ^{12}C/^{13}C = 9, 7, and 4. The best fit to the observed spectrum was achieved for ^{12}C/^{13}C = 7. A variation in ^{12}C/^{13}C only influences a little the theoretical profile of ^{12}CH 4210.9 Å, such that the C abundance obtained from fitting this line increases from $\log \varepsilon_{\rm C}$ = 7.44–7.54, when ^{12}C/^{13}C decreases from 95 (^{12}C fraction of 98.965 per cent) to 4 (^{12}C fraction of 80 per cent).

A supersolar fraction of the ^{13}C isotope can be a signature of AGB nucleosynthesis (e.g. Karakas 2010; Lugaro et al. 2012; Ventura et al. 2021). Here, the donor AGB star would likely have been of intermediate-mass ($M \gtrsim 2\,M_\odot$), such that it experienced proton capture nucleosynthesis at the convective envelope, leading to a low ^{12}C/^{13}C ratio and a large overabundance of N. Such stars are important contributors to ^{13}C and N in the early Galaxy (Kobayashi, Karakas & Lugaro 2020). Low-metallicity AGB stars can also produce large overabundances of O, which are dredged to the surface alongside C and heavy elements (Karakas 2010; Lugaro et al. 2012).

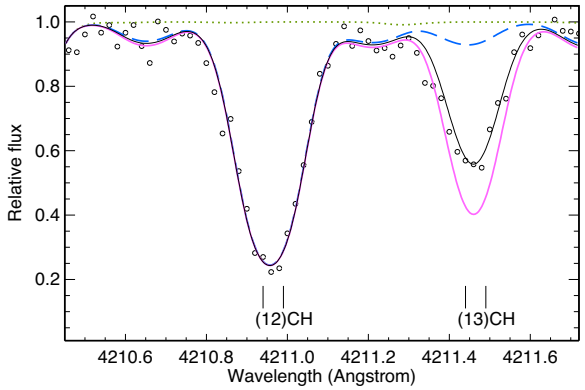

Figure 3. Molecular ^{12}CH and ^{13}CH (denoted as (12)CH and (13)CH) lines in spectrum of Pr184237 (open circles). The best fit (continuous curve) to the observations was achieved for the $^{12}C/^{13}C = 7$ isotopic ratio and $\log \varepsilon_C = 7.49$. The blue dashed and magenda three-dot–dashed curves correspond to $^{12}C/^{13}C = 95$ (the solar ratio) and 4, respectively. In two latter cases, the total carbon abundances are $\log \varepsilon_C = 7.44$ and 7.54.

With $T_{\rm eff} = 5100$ K and $\log g = 2.0$, Pr184237 is far from the AGB evolutionary phase, and the self-pollution hypothesis should be rejected. Variations in the radial velocity suggest binarity of the system, where Pr184237 is a less massive secondary component. The primary evolved to the AGB phase and via the mass transfer provided Pr184237 with the nuclear-processed material. At present, the primary is, probably, a white dwarf.

5.2 Elements Na to Zn

Lines of the four α-process elements, namely, Mg I, Si I, Ca I, and Ti II are measured in the spectrum of Pr184237. The star reveals an α-enhancement with tight measurements of [X/Fe] = 0.48, 0.36, 0.47, and 0.42, respectively. These numbers correspond to the NLTE calculations.

Pronounced NLTE effects are found for the resonance lines of Na I and Al I, such that NLTE leads to the lower abundance of Na compared with the LTE case, by 0.57 dex, and, in contrast, to a higher abundance of Al, by 0.45 dex. Red wings of the Na I 5889 and 5895 Å lines in spectrum of Pr184237 are affected by interstellar absorption lines, and we can only evaluate an upper limit for the element abundance: [Na/Fe] ≤ -0.3 in the NLTE calculations. It is important to note that Na is certainly depleted relative to Fe and does not follow the enhanced carbon. Aluminum does not reveal a notable deviation from the scaled solar abundance, with [Al/Fe] $= -0.06$ in the NLTE calculations.

Abundances of Sc and V were determined from lines of their majority species, Sc II and V II, which are expected to be weakly affected by the departures from LTE. Indeed, the NLTE calculations resulted in $\Delta_{\rm NLTE} < 0.01$ dex for the Sc II 4246 Å line observed in Pr184237. Scandium appears to be enhanced relative to Fe to the same extent, as are the α-process elements. Vanadium follows iron, with [V/Fe] $= -0.08$.

Abundances of Cr, Mn, Co, and Ni were derived from lines of their minority species, which are subject to the ultraviolet overionization, resulting in weakened lines and positive NLTE abundance corrections. For Cr I and Mn I, the NLTE corrections are available in the data base NLTE_MPIA[6] (Kovalev et al. 2018). They were computed based on the methods of Bergemann & Cescutti (2010) and Bergemann et al. (2019), respectively. For the atmospheric parameters of Pr184237, we extracted $\Delta_{\rm NLTE} = 0.56$ dex, 0.58 dex, 0.48 dex, and 0.26 dex for Cr I 4254, 4274, 5409 Å, and Mn I 4033 Å, respectively, and obtained [Cr/Fe](NLTE) = 0.33 and [Mn/Fe](NLTE) $= -0.20$. Thus, manganese in Pr184237 is deficient relative to Fe, independent of whether we rely on NLTE or LTE. Overabundance of Cr relative to Fe is unlikely. When taking the Cr I- and Fe I-based LTE abundances, we obtained a close-to-solar ratio of [Cr I/Fe I] $= -0.09$.

For the Co I lines, the NLTE corrections are not available in Bergemann, Pickering & Gehren (2010) and, currently, not accessible at the above cited website. However, they are certainly positive. Therefore, cobalt is enhanced in Pr184237, at the level of [Co/Fe] > 0.2.

When taking the LTE abundances from lines of Ni I and Fe I, we obtained [Ni I/Fe I] $= -0.07$, suggesting that the Ni abundance in Pr184237 is close to the scaled solar one.

Zinc is slightly enhanced, with [Zn/Fe](NLTE) = 0.21.

5.3 Neutron-capture elements Sr to Pb

We determine abundance for 15 elements beyond Sr (hereafter, heavy elements). Seven of them, namely, Sr, Y, Zr, Ba, La, Ce, and Pb, are commonly referred to as s-process elements because of the dominant contribution of the s-process to their solar abundances, of greater than 60 per cent according to Bisterzo et al. (2014). Five measured elements, namely, Eu, Gd, Dy, Er, and Tm, are presumably of r-process origin, with more than 80 per cent contribution of the r-process to their solar abundances. The remaining elements Nd, Sm, and Yb are intermediate cases, with approximately equal contributions of the r- and s-process to their solar abundances.

For Sr to Er, their abundances are derived from two to ten lines. The best fits to the representative lines are shown in Fig. 4. Ytterbium is observed in the only line, Yb II 3694 Å, and the only unblended line was found for Tm II.

A challenge was to determine the Pb abundance from the Pb I 4057 Å line, which is heavily blended by the molecular CH line. As shown in Fig. 5 (top panel), there are three unblended or weakly blended lines of ^{12}CH in the 4058.0–4059.7 Å range. They all are well fitted with $\log \varepsilon_C = 7.58$, which agrees within 0.06 dex with the C abundance derived from the C_2 Swan band. We note that the ^{13}CH 4058.448 Å line is reproduced reasonably well using $^{12}C/^{13}C = 7$, as derived in this study. It is evident that neither the position, nor the total absorption of the 4057 Å blend can be reproduced in the case of [Pb/Fe] = 0 ($\log \varepsilon_{\rm Pb} = -0.57$). In the LTE calculations, the best fit to the 4057 Å blend is achieved with $\log \varepsilon_{\rm Pb} = 1.55$. The obtained Pb abundance is supported by another line of Pb I, at 3683 Å. This line is located in a rather crowded region (Fig. 5 bottom panel), which is never the less well-fitted using the derived atmospheric parameters (important for H I 3682.8 Å!) and abundances of C and Fe. For Pb I 3683 Å, we show the synthetic profiles computed with [Pb/Fe] = 0, 1, and 2.12. It is evident that the first two profiles are too shallow compared with the observed one. Only Pb I 4057 Å was used to represent in Table 5 the systematic uncertainties in the Pb abundance. When varying $T_{\rm eff}$ or $\log g$ or ξ_t, we first evaluated the C abundance from the CH 4058.2, 4059.2, and 4059.5 Å lines, and then the Pb abundance was obtained from fitting the 4057.7 Å blend.

We obtain that elements of the second s-process peak (Ba, La, and Ce) and elements of the intermediate group (Nd, Sm, and Yb)

[6] http://nlte.mpia.de/

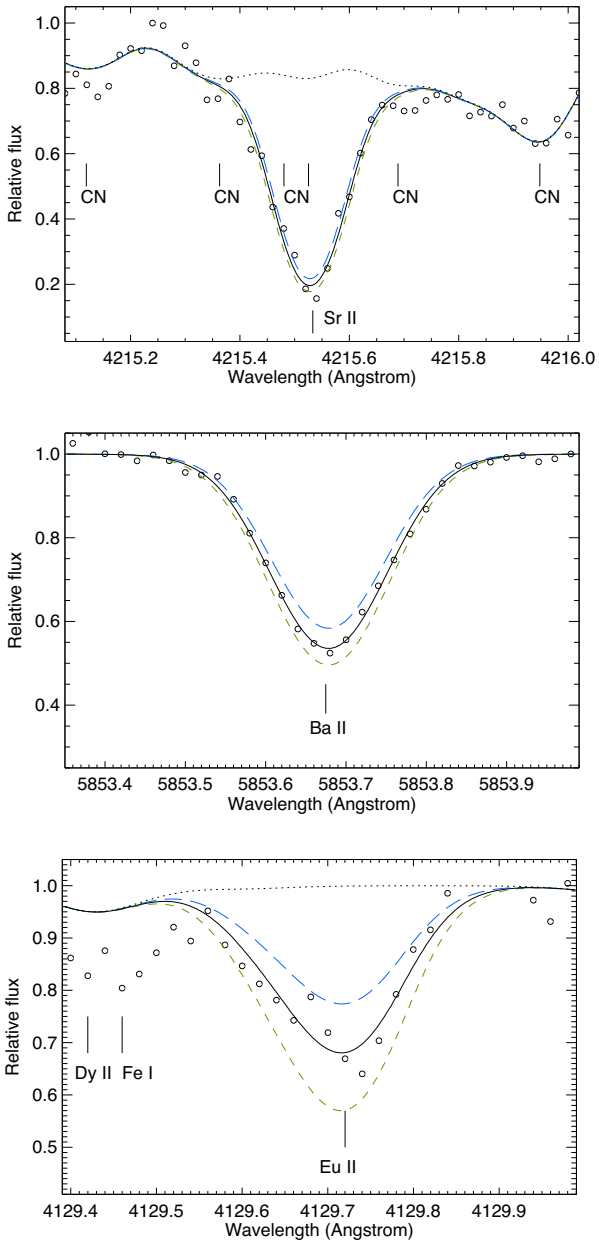

Figure 4. Best fits (continuous curve) to the Sr II 4215 Å (top panel), Ba II 5853 Å (middle panel), and Eu II 4129 Å (bottom panel) lines in Pr184237 (open circles). The derived abundances are indicated in Table 2. The dotted curves in the top and bottom panels show the synthetic spectra with no Sr and Eu in the atmosphere. The blue long-dashed and green short-dashed curves show the effect of a 0.2 dex variation in the abundance on the synthetic spectrum.

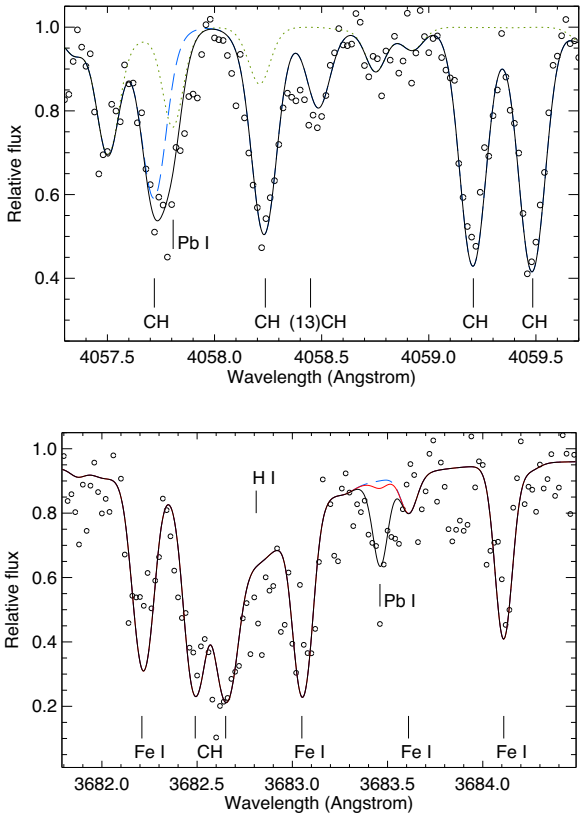

Figure 5. Best fits (continuous curve) to the Pb I 4057 Å (top panel) and 3683 Å (bottom panel) lines in Pr184237 (open circles). The derived abundances are indicated in Table 2. The blue dashed curves show the synthetic spectra computed with [Pb/Fe] = 0. The red dash–dotted curve in the bottom panel corresponds to [Pb/Fe] = 1.0. The green dotted curve in the top panel shows the synthetic spectrum computed without carbon in the atmosphere.

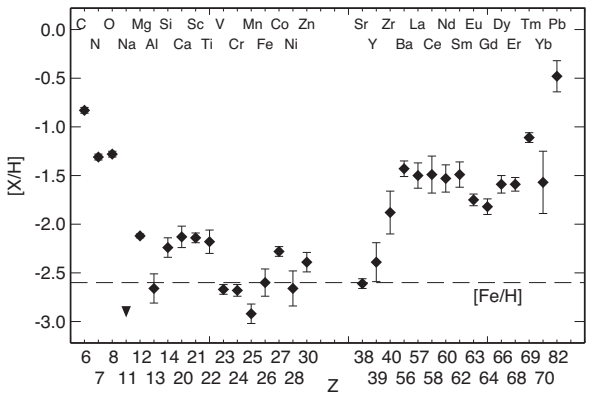

Figure 6. The element abundance pattern of Pr184237. An upper limit for the Na abundance is indicated by downward-facing triangle. The dashed line indicates the star's iron abundance [Fe/H] = −2.60. Abundances of Cr, Mn, Co, and Ni are increased by 0.14 dex, see text for more details.

are strongly enhanced in Pr184237, with [X/Fe] >1. An even higher excess was found for Pb, with [Pb/Fe] = 2.12 and 2.78 in the LTE and NLTE calculations, respectively.

Pr184237 is the first star in the inner Galaxy for which the five r-process elements are measured, and they all reveal an enhancement, with the average [r/Fe] = 1.03 ± 0.28.

The obtained element abundance pattern of Pr184237 is presented in Fig. 6. For illustration purpose, the LTE abundances of Cr, Mn, Co, and Ni were increased by 0.14 dex, which is the difference between the NLTE and LTE abundances for Fe I. By doing so, we assumed similar NLTE effects for neutral species of these five elements and, in the first approximation, accounted for the NLTE effects for Cr I, Mn I, Co I, and Ni I. For all elements beyond Sr, the LTE abundances are used for consistency.

5.4 Comparisons with the VMP stellar samples

For abundance comparisons, we use the VMP stellar samples observed towards the bulge from high-resolution spectroscopic studies of Howes et al. (2016), Koch et al. (2016), and Sestito et al. (2023).

Both Koch et al. (2016) and Sestito et al. (2023) conclude that the majority of their carbon-normal stars exhibit abundance patterns typical for the Galactic halo stars, although the [Na/Mg] ratios in Sestito et al. (2023) reveal a substantial star-to-star scatter. In contrast, Howes et al. (2016) find that the chemistry of their sample stars deviates from that for halo stars of the same metallicity. However, we see in their figs 11–13 that most of the elemental ratios lie well on the halo abundance trends. The star-to-star scatter is, indeed, observed for [Mg/Fe]. In the Na–Zn range, our CEMP star Pr184237 does not look exceptional among the non-CEMP stars.

Compared with the three carbon and s-process enhanced stars from Koch et al. (2016) and Sestito et al. (2023), Pr184237 has the lowest [Ba/Fe] = 1.17, however, this is the first star discovered in the inner Galaxy that is strongly enhanced in both s- and r-process elements. Not only Eu, but also Gd, Dy, Er, and Tm were measured in this star. With [Ba/Eu] = 0.32, Pr184237 likely belongs to the CEMP-r/s subclass.

Pr184237 is the only CEMP star in the inner Galaxy, for which the isotope abundance ratio $^{12}C/^{13}C$ and the Pb abundance are derived. Earlier, the Pb abundance, [Pb/Fe] = 1.50, was measured for a more metal-rich and non-CEMP star with [Fe/H] = −1.5 and [C/Fe] = 0.4 (Koch et al. 2019).

In order to compare Pr184237 with the Galactic halo CEMP-s and CEMP-r/s stars, we used the Stellar Abundances for Galactic Archaeology (SAGA) data base (Suda et al. 2008). In total, 58 stars were selected with [Fe/H] <−1.5, [C/Fe] >0.7, and the Pb abundance measured. We separated them into two subclasses, using the criteria by Beers & Christlieb (2005), namely, [Ba/Fe] >1 and [Ba/Eu] >0.5 for CEMP-s and [Ba/Eu] = 0 to 0.5, [Ba/Fe] >0 and [Eu/Fe] >0 for CEMP-r/s. The obtained subsamples of 24 CEMP-s and 18 CEMP-r/s stars, as well as the remaining CEMP stars with unknown Eu abundance are displayed together with Pr184237 in Fig. 7. The three groups of stars fully overlap on the abundance diagrams [Pb/Ba] and [Sr/Ba] versus [Ba/H]. The position of Pr184237 in these diagrams does not contradict either the CEMP-s or the CEMP-r/s status. Only the lower [Ba/Eu] ratio compared to the criterion for the CEMP-s subclass leads us to refer to Pr184237 to as a CEMP-r/s star.

6 ORIGIN OF THE HEAVY ELEMENT ABUNDANCE PATTERN

One commonly believes that the first heavy element nuclei in our Galaxy were produced in the r-process, although astrophysical sites for the r-process are still debated (see Cowan et al. 2021, for a thorough review). In the Galactic halo, a contribution of the main s-process to heavy element production becomes notable in stars starting from [Fe/H] ≃ −2.6, according to Simmerer et al. (2004), or even from higher [Fe/H] ≃ −1.4 (Roederer et al. 2010).

Spectroscopic analyses of MP stars in the inner Galaxy provide signatures of early r-process nucleosynthesis. Johnson, McWilliam & Rich (2013) and Howes et al. (2015, 2016) report on europium enhancements at the level of [Eu/Fe] = 0.5–1.0. Some of the stars, for example, 2MASS 18174532–3353235 ([Fe/H] = −1.67, [Eu/Fe] = 0.99, and [Ba/Eu] = −0.5, Johnson et al. 2013) and J181505.16-385514.9 ([Fe/H] = −3.29, [Eu/Fe] = 0.96, and [Ba/Eu] = −0.92, Howes et al. 2015), can be referred to as strongly r-process enhanced (r-II) stars, following the classification of Beers & Christlieb (2005). As shown by Johnson et al. (2012), Van der Swaelmen et al. (2016), and Forsberg et al. (2019, 2023), the r-process was the dominant neutron-capture production process in the bulge until metallicity reached [Fe/H] ∼ −1.

Therefore, we have every reason to believe that Pr184237 has formed from the matter where the heavy elements were of the r-process origin. Later the star's atmosphere was enriched with the nuclear-processed material transferred from the evolved companion. The enrichment scenario should explain enhanced abundances of the heavy elements and also enhancements in C, N, O and the low $^{12}C/^{13}C$ isotope ratio.

6.1 Pollution by the s-process products

In this scenario, we assume that heavy elements in Pr184237 originate from two sources. The first one is the interstellar matter out of which Pr184237 has formed, and it has the r-process element abundance pattern, with [r/Fe] = 1.03, as shown in Section 5.3. The second one is the s-process enriched material transferred on to a surface of Pr184237 from the more massive primary component when it evolved to the AGB phase. The transferred material was diluted with the atmospheric matter.

Initial abundances of the heavy elements in Pr184237, ε_r, were calculated using the empirical r-process relative yields, which were obtained from abundance analysis of a benchmark r-II star CS 31082-001 (Siqueira Mello et al. 2013). The r-II stars reveal very similar heavy element abundance patterns (Sneden, Cowan & Gallino 2008), suggesting a universal r-process. In Fig. 8, the heavy element abundance pattern of Pr184237 is displayed together with the scaled abundances of CS 31082-001. The scaling factor was calculated from matching the Eu abundances of Pr184237 and CS 31082-001. Abundances of Eu, Gd, Dy, and Er in Pr184237 lie well on the empirical r-process curve, suggesting an origin of these elements in the r-process. The Tm abundance, which is also expected to be on the r-process curve, appears to be higher. Three of the four inspected lines of Tm II, at 3700, 3701, and 3848 Å, are heavily affected by noise in the spectrum of Pr184237, and the abundance from Tm II 3795 Å seems to be overestimated. Neglecting Tm due to the uncertainty in its abundance, we computed the average [r/Fe] = 0.91 ± 0.12.

For the s-process abundances, ε_s, we used models of the s-process in the low-metallicity ([Fe/H] = −2.3) AGB stars computed by Lugaro et al. (2012) in the broad range of stellar masses (0.9–6 $M_\odot$) by varying the size of the ^{13}C pocket, which is an uncertain parameter in AGB nucleosynthesis.

The quality of each enrichment scenario was judged in terms of the χ^2 statistics. The statistical estimator is determined by

$$\chi^2 = \sum (\log \varepsilon_{obs} - \log \varepsilon_{mod})^2 / \sigma_{obs}^2, \quad (1)$$

where $\varepsilon_{mod} = d \cdot \varepsilon_r + (1 - d) \cdot \varepsilon_s$, d is a dilution factor, which is a free parameter and takes a value between 0 and 1, σ_{obs} is the abundance error, and the summation is carried out for the 15 elements from Sr to Pb observed in Pr184237.

Lugaro et al. (2012) provide two grids of the s-process abundances computed with two independent stellar evolution codes, STARS and Stromlo. For the first grid, the best fit to the observations, with χ^2 = 210 and d = 0.982, was obtained using the model with an initial mass of M_{init} = 2 $M_\odot$ and the mass of the partial mixing zone M_{mix} = 0.004 $M_\odot$. Note that the ^{13}C pocket forms in the partially mixed zone; we refer to Lugaro et al. (2012) for further details. In the Stromlo grid, the best model (χ^2 = 200, d = 0.980) has M_{init} = 1.5 $M_\odot$ and M_{mix} = 0.002 $M_\odot$. Both models are shown in Fig. 9

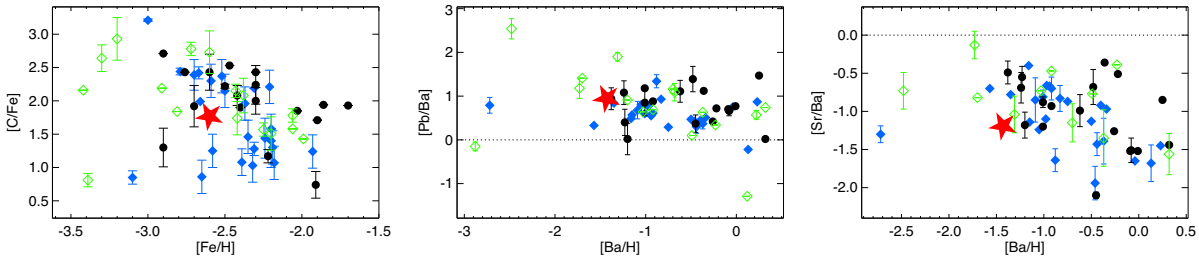

Figure 7. CEMP-s (blue filled diamonds), CEMP-r/s (filled circles), and the stars with unknown Eu abundance (open green diamonds) in the abundance diagrams [C/Fe] versus [Fe/H] (left-hand panel), [Pb/Ba] versus [Ba/H] (middle panel), and [Sr/Ba] versus [Ba/H]. The data are taken from the SAGA data base (Suda et al. 2008). Pr184237 is shown by the red star symbol.

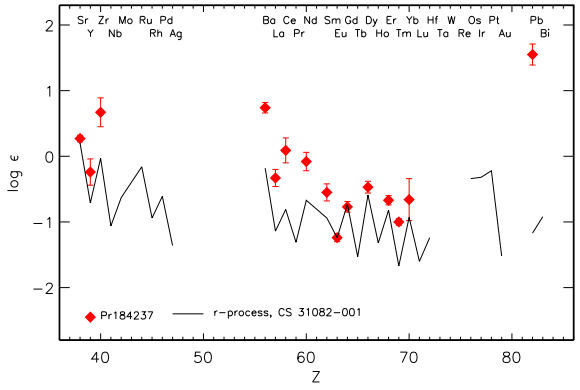

Figure 8. Heavy element abundance pattern of Pr184237 (diamonds) compared to abundances of an r-II star CS 31082-001 from Siqueira Mello et al. (2013). Abundances of CS 31082-001 were scaled to match the Eu abundance of Pr184237.

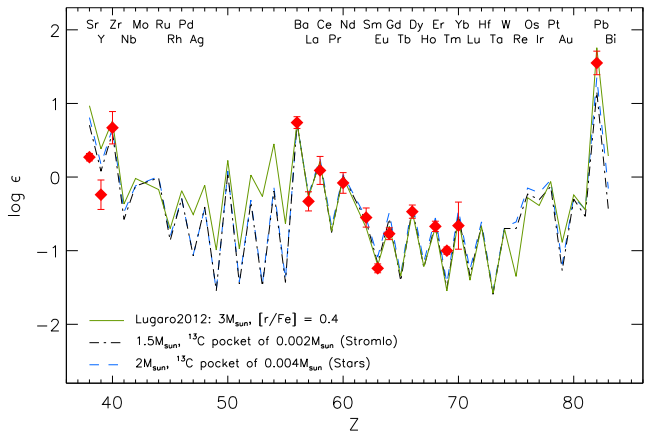

Figure 9. Heavy element abundance pattern of Pr184237 (diamonds) compared to different s-process models from Lugaro et al. (2012). See the text for more details.

compared with the observations.

Lugaro et al. (2012) computed also the models with the assumption that an initial composition of the stars producing s-nuclei was different from a scaled solar composition. Namely, the matter was r-process enriched with [r/Fe] = +0.4, +1.0, and +2.0. We neglect the models with [r/Fe] = + 2.0, because the binary components should have common initial abundances, but Pr184237 does not reveal such a strong r-process enhancement. The other models are checked by adopting $\varepsilon_{\rm mod} = \varepsilon_{\rm s}$. The best fit model ($\chi^2$ = 331) shown in Fig. 9 has M_{init} = 3 M$_\odot$, M_{mix} = 0.0005 M$_\odot$, and [r/Fe] = + 0.4.

Judging by a purely numerical criterion, the Stromlo model of M_{init} = 1.5 M$_\odot$, with the least χ^2 = 200, can be considered as the 'best model'. However, it overpredicts abundances of Sr and Y. This is in line with Lugaro et al. (2012), who conclude that the light-s/heavy-s element abundance ratios in their models are too high compared with the observations of CEMP-r/s stars. In contrast, the Pb abundance of the 'best model' is lower compared with that for Pr184237. The observed Pb abundance is reproduced by the higher mass models, namely, of 2 M$_\odot$ in the STARS grid and of 3 M$_\odot$ in the grid of the r-process enhanced models. Carbon enhancement of Pr184237 ([C/Fe] = 1.77) is reasonably well reproduced by each of three selected models ([C/Fe] = 1.51–1.94), when applying the dilution factor obtained in fitting the heavy element abundance pattern and assuming the initial C abundance to be equal to the scaled solar one. However, the predicted ^{12}C/^{13}C isotope ratio is supersolar, in contrast to our finding for Pr184237.

6.2 Pollution by the i-process products

It is possible to reproduce the observed abundances of CEMP-r/s stars by using nucleosynthesis models for the intermediate (i) neutron capture process (Dardelet et al. 2014; Hampel et al. 2016, 2019; Goswami et al. 2021). This nucleosynthesis process introduced first by Cowan & Rose (1977) runs at neutron densities of $N_{\rm n}$ = 10^{11}–10^{15} cm^{-3}, which are intermediate to that of the main s-process, which typically occurs at $N_{\rm n} \lesssim 10^8$ cm^{-3}, and considerably lower than r-process neutron densities. While He-shell burning in intermediate-mass AGB stars can result in $N_{\rm n} \sim 10^{12}$ cm^{-3} (Fishlock et al. 2014), owing to the operation of the ^{22}Mg(α,n)^{25}Mg reaction, the neutron exposure (Busso, Gallino & Wasserburg 1999) is likely not high enough to initiate an i-process. The operation of the i-process can produce enhancements in elements typically produced by both the s- and r-process (e.g. Ba and Eu), although the resulting abundance distribution is unique and not a superposition of the two (Hampel et al. 2019). Favourable conditions for the i-process can be found in multiple stellar sites, for example, proton-ingestion episodes (PIEs) in AGB stars, super-AGB stars, and RAWD (see, for example Hampel et al. 2016, 2019; Denissenkov et al. 2017, 2019; Choplin, Siess & Goriely 2021, 2022).

In order to understand an origin of the heavy elements in Pr184237, we explore the i-process nucleosynthesis in AGB stars, using the models of Hampel et al. (2019) and Choplin et al. (2022), and in RAWD, using the models of Denissenkov et al. (2019). In the AGB star scenario, the investigated star is in a binary system and has accreted the i-process material from the AGB companion (which is now a white dwarf). In the scenario of enrichment of Pr184237 with the i-process products from the RAWD, the investigated star would have been a low-mass third companion orbiting the close, previously

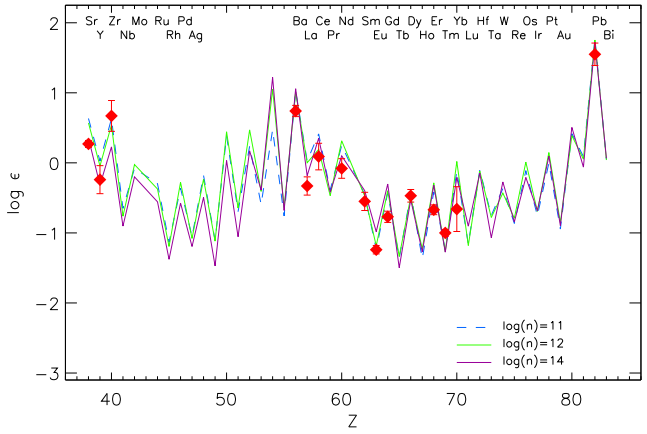

Figure 10. Heavy element abundance pattern of Pr184237 (diamonds) compared to the best fit i-process models calculated following Hampel et al. (2019).

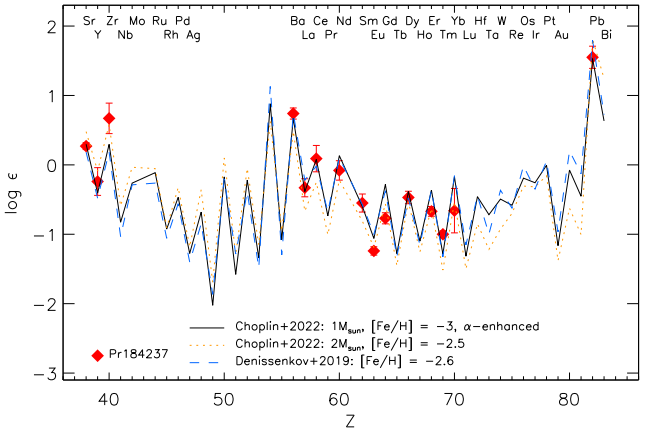

Figure 11. Heavy element abundance pattern of Pr184237 (diamonds) compared to the models of an i-process nucleosynthesis in the AGB star (Choplin et al. 2022, continuous and dotted curves for two models) and the RAWD (Denissenkov et al. 2019, dashed curve). See text for more details.

interacting, binary system with the RAWD. Denissenkov et al. (2019) proposed that the i-process enriched star would have accreted a wind material ejected by the RAWD. There are two possible scenarios: either the RAWD exploded as a type Ia supernova (SN Ia), and the i-process enriched star was ejected from the triple system, or it did not explode and the i-process enriched star is still part of the triple system. Variations in the radial velocity of Pr184237 suggest that our star could still orbit the surviving component in this scenario.

For each of the i-process models, we assume some dilution of the produced i-process nuclei with the heavy elements of the atmospheric matter, such that $\varepsilon_{\rm mod}$ in formula (1) is determined by

$$\log \varepsilon_{\rm mod} = \log(d \cdot \varepsilon_{\rm init} + (1-d) \cdot \varepsilon_{\rm i-proc}), \quad (2)$$

where $\varepsilon_{\rm i\text{-}proc}$ is the i-process abundance of a given element, $\varepsilon_{\rm init}$ is the initial atmospheric abundance, and d is a dilution factor. The model abundances are fitted to the abundances of 15 heavy elements observed in Pr184237.

In Fig. 10, we show the results from Hampel et al. (2019) of an i-process calculated with constant neutron densities of different magnitude. The calculations assume conditions typical of the inter-shell region of a low-mass, low-metallicity AGB star. In the fitting procedure, the scaled solar abundances were adopted as $\varepsilon_{\rm init}$. The best three fits correspond to $N_{\rm n} = 10^{11}$ cm^{-3} ($\chi^2 \simeq 107$), 10^{12} cm^{-3} ($\chi^2 \simeq 115$), and 10^{14} cm^{-3} ($\chi^2 \simeq 117$), although qualitatively the fits look similar. Differences show up in the region between Sr and Ba, which are elements not observed for Pr184237.

Choplin et al. (2022) calculated 12 stellar evolution models with various initial masses and metallicities. Proton ingestion events happen in six of them, namely, in 1 and 2 M$_\odot$ AGB models with [Fe/H] $= -3$, -2.5, and -2.3. The companion to Pr184237 had enough time to evolve to the AGB phase. Choplin et al. (2022, table 1) predicted total lifetimes of 6.3 and 0.8 Gyr for the $M = 1$ and 2 M$_\odot$ models, respectively. When fitting the i-process yields to the observed heavy element abundance pattern, we assume that they are diluted with $\varepsilon_{\rm init} = \varepsilon_{\rm r}$. Here, $\varepsilon_{\rm r}$ is determined as in the previous subsection. We obtain that the model with $M_{init} = 1$ M$_\odot$, [Fe/H] $= -3$, and α-enhancement (M1.0z3.0a) has the smallest $\chi^2 = 109$ ($d = 0.98$) and reproduces well the heavy element abundance pattern of Pr184237, including the light neutron-capture elements Sr and Y (Fig. 11). There are a few subtle differences though for the r-process elements Gd, Dy, Er and also for Zr and Yb. This model predicts two pulses, and the PIE arises during the second one, such that the AGB surface is enriched in i-process products right after the PIE. With the dilution factor $d = 0.98$ and the scaled solar abundance as the initial C abundance, the M1.0z3.0a model predicts the present C enhancement as [C/Fe] $= 1.42$, which is slightly less than the observed value, and the isotope ratio of ^{12}C/^{13}C $= 4.3$, which is close to the observed value.

Fig. 11 also shows the model for 2 M$_\odot$ and [Fe/H] $= -2.5$ (M2.0z2.5). Keeping in mind that the Tm abundance of Pr184237 seems to be overestimated (see Section 6.1), we find the best fits to the observed abundance pattern that does not include Tm. The lowest $\chi^2 = 54.7$ ($d = 0.95$) was obtained for the M2.0z2.5 model. However, the M1.0z3.0a model has a similarly small $\chi^2 = 58.4$ ($d = 0.985$). Compared to M1.0z3.0a, the M2.0z2.5 model reproduces well observed abundances of Eu to Yb (Tm is not included) and not only Sr and Y, but also Zr. However, M2.0z2.5 is worse for Ba, La, Ce and, with ^{12}C/^{13}C $= 24.5$, also for the carbon isotope ratio. Right after the PIE pulse the model predicts low ^{12}C/^{13}C $= 3.5$, but an enrichment of the AGB surface in ^{13}C reduces during ten subsequent thermal pulses due to a dilution of the i-process material.

For an i-process in RAWD, we use the G (iRAWD_2.6) model of Denissenkov et al. (2019) with exactly the same metallicity as [Fe/H] $= -2.6$ for Pr184237. They calculated an evolution of a close binary system with $M_1 = 2.5$ M$_\odot$ and $M_2 = 2.0$ M$_\odot$ and the i-process nucleosynthesis when the primary reached the stage of RAWD. The best fit ($\chi^2 = 119$) displayed in Fig. 11 was obtained with a dilution factor of $d = 0.9997$. The RAWD model predicts slightly greater [C/Fe] $= 2.02$ value than the observed C enhancement, but extremely high ^{12}C/^{13}C isotope ratio.

6.3 Uncertainties in the choice of enrichment scenario

In all of the considered scenarios, the initial atmospheric chemical composition of Pr184237 is polluted by nucleosynthesis products transferred from the more massive, evolved companion. Can we decide on the type of nucleosynthesis and initial mass of the companion from a comparison of our observed data with the theoretical models?

Compared with an i-process, we have more arguments against the s-process enrichment. The best fit s-process models have greater χ^2, by a factor of more than two. This is mostly due to the overproduction of the light neutron-capture elements Sr and Y. When ignoring Sr to Zr, we obtained $\chi^2 = 119$ for the Stromlo model of 1.5 M$_\odot$

shown in Fig. 9. The s-process models produce a C enhancement close to the observed one, but with much lower enhancements in N and O. For example, assuming the initial abundances [N/Fe] = 0 and [O/Fe] = 0.5, we obtain [N/Fe] = 0.14 and [O/Fe] = 0.68 after the pollution. To remind the reader, Pr184237 reveals [N/Fe] = 1.29 and [O/Fe] = 1.32. The s-process models predict very high $^{12}C/^{13}C$ isotope ratios, however, this and the low [N/Fe] predicted from the model can be due to uncertainties in the theoretical models of low-metallicity AGB stars.

Of two sites for an i-process, AGB and RAWD, no preference can be given to any of them with respect to χ^2 and enhancements in C, N, and O. For Pr184237, we derive supersolar and similar [C/N] and [C/O] ratios at the level of 0.45. Supersolar [C/O] $\simeq$ 0.3 ratios are predicted by the M1.0z3.0a and M2.0z2.5 models of Choplin et al. (2022) and the iRAWD_2.6 model of Denissenkov et al. (2019). The initial O abundance was assumed to be [O/Fe] = 0.5. There are discrepancies in [C/N] between the models and observations, however, we realize that our estimate of the N abundance in Pr184237 is less reliable compared with that for C and O.

From a chemistry point of view, an advantage of the AGB i-process models of Choplin et al. (2022) is a subsolar $^{12}C/^{13}C$ ratio at the surface of the polluted star, which tends to be in line with observations of Pr184237.

We realize that our conclusion about a preferable enrichment scenario can be influenced by the uncertainties in the theoretical models and in the element abundances determined for Pr184237.

6.3.1 *Uncertainties in modelling the i-process*

Theoretical modelling of low and intermediate-mass stars on the AGB comes with significant uncertainties when considering mixing between the He-shell and envelope, and from mass-loss, some of which is likely accreted on to the companion by stellar wind accretion. For low-metallicity AGB stars the situation is even more complicated owing to PIEs, which can drive an i-process, along with the previous uncertainties (we refer to Karakas & Lattanzio 2014, for a detailed discussion). Choplin et al. (2021) perform detailed AGB calculations of proton-ingestion and found that the event can terminate the AGB phase, a phenomenon not found by Campbell & Lattanzio (2008). However Choplin et al. (2021) have coupled the surface opacity to the envelope enrichment, which affects the structure significantly after the star becomes carbon rich (e.g. see also Marigo 2002). These authors also examine the effect of modelling uncertainties on the nucleosynthesis predictions and note an uncertainty of $\pm$0.3 dex in the abundances. This value does not take uncertainties from nuclear physics into consideration, where many nuclei are unstable and consequently have uncertain neutron capture cross-sections.

An impact of the uncertainties in the (n,γ) reaction rates and β-decay rates for 164 unstable isotopes, from ^{131}I to ^{189}Hf, on the predicted i-process abundances was investigated by Denissenkov et al. (2021) with their RAWD ([Fe/H] = $-$2.6) model for the elements from Ba to W. Denissenkov et al. (2021) show that variations in the (n,γ) reaction rates result in notable changes of up to 0.5 dex (see their figs 7, 10, and 15) in the predicted abundances.

For the RAWD model from Denissenkov et al. (2019), the main uncertainty is that the mass accretion rate is held steady at a low value, which leads to H-flashes that cause the envelope of the accreted matter to expand. In order to stop the model from becoming a red giant, an artificial mass-loss is assumed to bring the model back to a steady mass accretion. Secondly, the low-metallicity WDs tend to grow significantly, nearing the Chandrasekhar limiting mass and may explode as a type Ia supernova. While low-metallicity SNeIa likely occurred, they must have been very rare in the early Universe or we would see evidence of this in the chemical record (e.g. lower [α/Fe], higher Mn abundance, etc). Côté et al. (2018) studied the i-process contribution from RAWDs to the chemical enrichment of the galaxy, and included an exploration of the number of RAWD systems using binary population synthesis. Interestingly in the binary population synthesis model, the systems that evolved to become RAWDs avoided SN Ia altogether, as a consequence of artificially suppressing H accumulation on to the WD. While this may avoid the issues discussed above in regard to low metallicity SN Ia, it also suggests that the WD growth seen in the models of Denissenkov et al. (2019) may not happen.

In summary, the i-process may have occurred in multiple stellar sites in the early Galaxy including low-metallicity AGB stars, rapidly rotating white dwarfs, and even perhaps massive stars (Banerjee, Qian & Heger 2018; Clarkson, Herwig & Pignatari 2018). It is unclear as yet, which of these sites polluted the stars with neutron-capture elements, with all sites still showing considerable uncertainties stemming from modelling and input physics.

6.3.2 *Uncertainties in the abundance determinations*

As already noted, we probably overestimate the Tm abundance. If we remove Tm from the the heavy element abundance pattern, the AGB star of not only $M_{\rm init}$ = 1.0, but also $M_{\rm init}$ = 2 M$_\odot$ can be the site of an i-process that enriched Pr184237. For the s-process models, removing Tm decreases χ^2, for example to χ^2 = 93.7 for the 1.5 M$_\odot$ shown in Fig. 9, but the best fit models remain the same.

The analysis of the enrichment scenarios was based on the LTE abundances of Pr184237. When using the NLTE abundances for Sr, Ba, Eu, and Pb and the LTE abundances for the remaining elements, we obtain slightly different χ^2 = 140 (d = 0.99995) for the iRAWD_2.6 model. In the case of the AGB i-process, the best fit (χ^2 = 110, d = 0.99) is achieved for the same mass (1.0 M$_\odot$), but a higher metallicity of [Fe/H] = $-$2.5. The best fits for the s-process models in the Stromlo grid are shifted to the higher masses of 2 and 2.5 M$_\odot$. We also made fitting the i-process models of Choplin et al. (2022) to the NLTE abundances of Sr, Ba, Eu, and Pb without including the other heavy elements and obtained the same solution for the best fit model, that is M1.0z2.5. NLTE leads to a 0.66 dex higher Pb abundance of Pr184237 compared with the LTE value, and none of the considered models predicts such a high Pb abundance. The difference between the observed and theoretical values amounts to 0.3 dex for the Choplin et al. (2022) model and exceeds 0.5 dex for the iRAWD_2.6 and the s-process models.

When fitting the i-process models of Choplin et al. (2022) and Denissenkov et al. (2019), we assume that the initial chemical composition has the r-process pattern. We tested whether using the scaled solar abundances, $\varepsilon_\odot$, can influence on the stellar parameters of the best fits. The present Solar system abundances were taken from Lodders (2021). The obtained results are very similar to that for $\varepsilon_{\rm init} = \varepsilon_{\rm r}$. The least χ^2 = 116 (d = 0.97) was achieved for the same AGB model of 1 M$_\odot$ and [Fe/H] = $-$3. The χ^2 slightly increases up to χ^2 = 122 (d = 0.9997) for the iRAWD_2.6 model.

Thus, an i-process nucleosynthesis in the AGB stars with a progenitor mass of 1.0–2.0 M$_\odot$, as calculated by Choplin et al. (2022), is a promising scenario to explain the CEMP-r/s phenomenon at the surface of Pr184237.

7 CONCLUSIONS

In a sample of 20 VMP stars selected from the PIGS survey for a high-resolution spectroscopic follow-up with UVES/VLT2, a FERRE analysis identified a CEMP star, Pr184237, which is strongly enhanced also in Ba, La, and Eu. Its orbit is confined to within ∼2.6 kpc of the Galactic centre, and it is most likely an early Milky Way star rather than accreted. In this study, we improved the star's atmospheric parameters: $T_{\rm eff}$ = 5100 K, $\log g$ = 2.0, and [Fe/H] = −2.60 and determined abundances of 32 chemical elements, including 15 heavy elements beyond the iron group. The atmospheric parameters and abundances of 13 elements, from Na to Pb, were derived based on the NLTE line formation.

We improved the C abundance, [C/Fe] = 1.77, and found that Pr184237 is also enhanced in N and O. The star reveals a low carbon isotope ratio of $^{12}C/^{13}C = 7$, which is a signature of nuclear-processed material. Pr184237 is far from the AGB evolutionary phase, and the self-pollution hypothesis should be rejected. The element abundance pattern in the Na–Zn range is typical of the Galactic halo stars. However, the neutron-capture elements, in particular lead with [Pb/Fe] = 2.12 (LTE) and 2.78 (NLTE), are strongly enhanced. With [Ba/Eu] = 0.32, Pr184237 is the first star of the CEMP-r/s subclass in the inner Galaxy. Compared with the halo CEMP-r/s stars, Pr184237 reveals very similar abundance ratios among the representative elements of the first, second and third s-process peaks, namely, Sr, Ba, and Pb.

We considered two scenarios of chemical enrichment for Pr184237. In both cases, the star is likely in a binary or higher order multiple system, consistent with the detected radial velocity variability.

In the first scenario, the star would have been born from the r-process rich material enriched by previous stellar generations, and would have been polluted with the s-process elements by a binary companion (former AGB) – this is the r + s scenario, where the different heavy elements come from different sources. We applied the empirical r-process yields based on abundances of an r-II star CS 31082-001 (Siqueira Mello et al. 2013) and the s-process abundances from calculations of metal-poor AGB stars by Lugaro et al. (2012) and fitted a combination of them. We find that some of the observed abundances of the first s-process peak elements (Sr, Y) cannot be explained in the r + s scenario. This scenario does not reproduce the subsolar $^{12}C/^{13}C$ isotope ratio derived for Pr184237.

In the second scenario, the initial chemical composition could be polluted with both s- and r-process elements produced by the i-process nucleosynthesis, which can occur in the companion AGB star or RAWD. We checked the i-process models from Hampel et al. (2019), Choplin et al. (2022) – both for AGB stars and Denissenkov et al. (2019, for RAWDs). For each grid, the best fit models reproduce reasonably well the heavy element abundance pattern of Pr184237. The models from Choplin et al. (2022) and Denissenkov et al. (2019) reproduce also the C enhancement and the C/O ratio. A subsolar $^{12}C/^{13}C$ isotope ratio is only obtained when using the AGB models of 1.0–2.0 $M_\odot$ from calculations of Choplin et al. (2022).

This study supports the hypothesis that the CEMP-r/s stars, like all CEMP-s stars, form in binary or higher order multiple system (see Abate et al. 2016; Goswami et al. 2021, and references therein). We consider an i-process nucleosynthesis in the AGB stars with a progenitor mass of 1.0–2.0 $M_\odot$ and a transfer of the nuclear-processed material on to the companion surface as a promising scenario for explaining the CEMP-r/s phenomenon of Pr184237. This suggests that the i-process could contribute to the chemical evolution of carbon and heavy elements in the inner Galaxy.

ACKNOWLEDGEMENTS

This study is based on observations made with the Very Large Telescope of the European South Observatory (Chile) under program ID 0105.B-0078(A). This research has made use of the data from the European Space Agency (ESA) mission Gaia,[7] processed by the Gaia Data Processing and Analysis Consortium (DPAC[8]). Funding for the DPAC has been provided by national institutions, in particular the institutions participating in the Gaia Multilateral Agreement. This research has made use of the data from the VALD, SAGA, and ADS[9] data bases. This research was enabled in part by support provided by BC DRI (British Columbia Digital Research Infrastructure) Group and the Digital Research Alliance of Canada.[10] AA acknowledges support from the Herchel Smith Fellowship at the University of Cambridge and a Fitzwilliam College research fellowship supported by the Isaac Newton Trust. DA acknowledges financial support from the Spanish Ministry of Science and Innovation (MICINN) under the 2021 Ramón y Cajal program MICINN RYC2021–032609. AIK was supported by the Australian Research Council Centre of Excellence for All Sky Astrophysics in 3 Dimensions (ASTRO 3D), through project number CE170100013. NFM gratefully acknowledges support from the French National Research Agency (ANR) funded project 'Pristine' (ANR-18-CE31-0017) along with funding from the European Research Council (ERC) under the European Unions Horizon 2020 research and innovation programme (grant agreement number 834148). FS thanks the Dr Margaret 'Marmie' Perkins Hess post-doctoral fellowship for funding his work at the University of Victoria. JIGH acknowledges financial support from the Spanish Ministry of Science and Innovation (MICINN) project PID2020-117493GB-I00.

Based on observations made with the Very Large Telescope (VLT).

8 DATA AVAILABILITY

All our main results are available in the tables in this article. The UVES spectrum is publicly available on the ESO archive. Other data underlying this article will be shared on reasonable request to the corresponding author.

REFERENCES

Abate C., Stancliffe R. J., Liu Z.-W., 2016, A&A, 587, A50
Aguado D. S., González Hernández J. I., Allende Prieto C., Rebolo R., 2017, A&A, 605, A40
Aguado D. S. et al., 2021a, MNRAS, 500, 889
Aguado D. S. et al., 2021b, ApJ, 908, L8
Alexeeva S., Pakhomov Y., Mashonkina L., 2014, Astron. Lett., 40, 406
Allende Prieto C., Beers T. C., Wilhelm R., Newberg H. J., Rockosi C. M., Yanny B., Lee Y. S., 2006, ApJ, 636, 804
Amarsi A. M., Nordlander T., Barklem P. S., Asplund M., Collet R., Lind K., 2018, A&A, 615, A139
Aoki W., Beers T. C., Christlieb N., Norris J. E., Ryan S. G., Tsangarides S., 2007, ApJ, 655, 492
Arentsen A. et al., 2020a, MNRAS, 491, L11
Arentsen A. et al., 2020b, MNRAS, 496, 4964
Arentsen A. et al., 2021, MNRAS, 505, 1239
Banerjee P., Qian Y.-Z., Heger A., 2018, ApJ, 865, 120
Beers T. C., Christlieb N., 2005, ARA&A, 43, 531
Belokurov V., Kravtsov A., 2022, MNRAS, 514, 689

[7] https://www.cosmos.esa.int/gaia
[8] https://www.cosmos.esa.int/web/gaia/dpac/consortium
[9] http://adsabs.harvard.edu/abstract_service.html
[10] https://alliancecan.ca

Bergemann M., Cescutti G., 2010, A&A, 522, A9
Bergemann M., Pickering J. C., Gehren T., 2010, MNRAS, 401, 1334
Bergemann M. et al., 2019, A&A, 631, A80
Bisterzo S., Travaglio C., Gallino R., Wiescher M., Käppeler F., 2014, ApJ, 787, 10
Bovy J., 2015, ApJS, 216, 29
Bridges J. M., 1973, in Štoll I., ed., Phenomena in Ionized Gases, Eleventh International Conference. IOP Publishing Ltd, Bristol, p. 418
Busso M., Gallino R., Wasserburg G. J., 1999, ARA&A, 37, 239
Butler K., 1984, PhD thesis, Univ. London
Campbell S. W., Lattanzio J. C., 2008, A&A, 490, 769
Chiappini C., Hirschi R., Meynet G., Ekström S., Maeder A., Matteucci F., 2006, A&A, 449, L27
Choplin A., Siess L., Goriely S., 2021, A&A, 648, A119
Choplin A., Siess L., Goriely S., 2022, A&A, 667, A155
Clarkson O., Herwig F., Pignatari M., 2018, MNRAS, 474, L37
Côté B., Denissenkov P., Herwig F., Ruiter A. J., Ritter C., Pignatari M., Belczynski K., 2018, ApJ, 854, 105
Cowan J. J., Rose W. K., 1977, ApJ, 212, 149
Cowan J. J., Sneden C., Lawler J. E., Aprahamian A., Wiescher M., Langanke K., Martínez-Pinedo G., Thielemann F.-K., 2021, Rev. Mod. Phys., 93, 015002
Dardelet L. et al., 2014, in XIII International Symposium on Nuclei in the Cosmos (NIC XIII), PoS, Trieste, Italy, p. 145
Denissenkov P. A., Herwig F., Battino U., Ritter C., Pignatari M., Jones S., Paxton B., 2017, ApJ, 834, L10
Denissenkov P. A., Herwig F., Woodward P., Andrassy R., Pignatari M., Jones S., 2019, MNRAS, 488, 4258
Denissenkov P. A., Herwig F., Perdikakis G., Schatz H., 2021, MNRAS, 503, 3913
Fishlock C. K., Karakas A. I., Lugaro M., Yong D., 2014, ApJ, 797, 44
Forsberg R., Jönsson H., Ryde N., Matteucci F., 2019, A&A, 631, A113
Forsberg R., Rich R. M., Nieuwmunster N., Jönsson H., Schultheis M., Ryde N., Thorsbro B., 2023, A&A, 669, A17
Frebel A., 2018, Ann. Rev. Nuc. Partic. Sci., 68, 237
Frebel A., Norris J. E., 2015, ARA&A, 53, 631
Gaia Collaboration et al., 2022, preprint (arXiv:2208.00211)
Giddings J., 1981, PhD thesis, Univ. London
González Hernández J. I., Bonifacio P., 2009, A&A, 497, 497
Goswami P. P., Rathour R. S., Goswami A., 2021, A&A, 649, A49
Green G. M., Schlafly E., Zucker C., Speagle J. S., Finkbeiner D., 2019, ApJ, 887, 93
Grevesse N., Sauval A. J., 1999, A&A, 347, 348
Gustafsson B., Edvardsson B., Eriksson K., Jorgensen U. G., Nordlund Å., Plez B., 2008, A&A, 486, 951
Hampel M., Stancliffe R. J., Lugaro M., Meyer B. S., 2016, ApJ, 831, 171
Hampel M., Karakas A. I., Stancliffe R. J., Meyer B. S., Lugaro M., 2019, ApJ, 887, 11
Hansen T. T., Andersen J., Nordström B., Beers T. C., Placco V. M., Yoon J., Buchhave L. A., 2016, A&A, 588, A3
Howes L. M. et al., 2015, Nature, 527, 484
Howes L. M. et al., 2016, MNRAS, 460, 884
Iben I. Jr, 1967, ApJ, 147, 624
Johnson C. I., Rich R. M., Kobayashi C., Fulbright J. P., 2012, ApJ, 749, 175
Johnson C. I., McWilliam A., Rich R. M., 2013, ApJ, 775, L27
Karakas A. I., 2010, MNRAS, 403, 1413
Karakas A. I., Lattanzio J. C., 2014, PASA, 31, e030
Kobayashi C., Karakas A. I., Lugaro M., 2020, ApJ, 900, 179
Koch A., McWilliam A., Preston G. W., Thompson I. B., 2016, A&A, 587, A124
Koch A., Reichert M., Hansen C. J., Hampel M., Stancliffe R. J., Karakas A., Arcones A., 2019, A&A, 622, A159
Kochukhov O., 2018, BinMag: widget for comparing stellar observed with theoretical spectra. Astrophysics Source Code Library
Koesterke L., Allende Prieto C., Lambert D. L., 2008, ApJ, 680, 764
Koleva M., Prugniel P., Bouchard A., Wu Y., 2009, A&A, 501, 1269
Lardo C. et al., 2021, MNRAS, 508, 3068
Lightkurve Collaboration et al., 2018, Lightkurve: Kepler and TESS time series analysis in Python. Astrophysics Source Code Library
Lodders K., 2021, Space Sci. Rev., 217, 44
Lucey M. et al., 2019, MNRAS, 488, 2283
Lugaro M., Karakas A. I., Stancliffe R. J., Rijs C., 2012, ApJ, 747, 2
Kovalev M, Brinkmann S., Bergemann M., MPIA IT-Department, 2018, NLTE MPIA web server, [Online]. Max Planck Institute for Astronomy, Heidelberg, last accessed date: October 28, 2022, http://nlte.mpia.de
Marigo P., 2002, A&A, 387, 507
Markwardt C. B., 2009, in Bohlender D. A., Durand D., Dowler P., eds, ASP Conf. Ser. Vol. 411, Astronomical Data Analysis Software and Systems XVIII. Astron. Soc. Pac., San Francisco, p. 251
Mashonkina L., 2013, A&A, 550, A28
Mashonkina L., 2020, MNRAS, 493, 6095
Mashonkina L. I., Belyaev A. K., 2019, Astron. Lett., 45, 341
Mashonkina L., Gehren T., 2000, A&A, 364, 249
Mashonkina L. I., Romanovskaya A. M., 2022, Astron. Lett., 48, 455
Mashonkina L., Christlieb N., Barklem P. S., Hill V., Beers T. C., Velichko A., 2010, A&A, 516, A46
Mashonkina L., Gehren T., Shi J.-R., Korn A. J., Grupp F., 2011, A&A, 528, A87
Mashonkina L., Ryabtsev A., Frebel A., 2012, A&A, 540, A98
Mashonkina L., Belyaev A. K., Shi J.-R., 2016a, Astron. Lett., 42, 366
Mashonkina L., Sitnova T., Pakhomov Y., 2016b, Astron. Lett., 42, 606
Mashonkina L., Jablonka P., Pakhomov Y., Sitnova T., North P., 2017a, A&A, 604, A129
Mashonkina L., Sitnova T., Belyaev A. K., 2017b, A&A, 605, A53
Mashonkina L., Pakhomov Y. V., Sitnova T., Jablonka P., Yakovleva S. A., Belyaev A. K., 2022, MNRAS, 509, 3626
Meléndez J., Barbuy B., 2009, A&A, 497, 611
Moity J., 1983, A&AS, 52, 37
Mucciarelli A., Bellazzini M., Massari D., 2021, A&A, 653, A90
Nomoto K., Kobayashi C., Tominaga N., 2013, ARA&A, 51, 457
Pakhomov Y. V., Ryabchikova T. A., Piskunov N. E., 2019, Astron. Rep., 63, 1010
Placco V. M., Frebel A., Beers T. C., Stancliffe R. J., 2014, ApJ, 797, 21
Raassen A. J. J., Uylings P. H. M., 1998, A&A, 340, 300
Rimoldini L. et al., 2022, preprint (arXiv:2211.17238)
Rix H.-W. et al., 2022, ApJ, 941, 45
Roederer I. U., Cowan J. J., Karakas A. I., Kratz K.-L., Lugaro M., Simmerer J., Farouqi K., Sneden C., 2010, ApJ, 724, 975
Ryabchikova T., Piskunov N., Kurucz R. L., Stempels H. C., Heiter U., Pakhomov Y., Barklem P. S., 2015, Phys. Scr, 90, 054005
Saunders W. et al., 2004, in Moorwood A. F. M., Iye M., eds, Proc. SPIE Conf. Ser. Vol. 5492, Ground-Based Instrumentation for Astronomy. SPIE, Bellingham, p. 389
Sbordone L., 2005, Memorie della Societa Astronomica Italiana Supplementi, 8, 61
Schlafly E. F., Finkbeiner D. P., 2011, ApJ, 737, 103
Schlegel D. J., Finkbeiner D. P., Davis M., 1998, ApJ, 500, 525
Sestito F. et al., 2019, MNRAS, 484, 2166
Sestito F. et al., 2023, MNRAS, 518, 4557
Simmerer J., Sneden C., Cowan J. J., Collier J., Woolf V. M., Lawler J. E., 2004, ApJ, 617, 1091
Siqueira Mello C. et al., 2013, A&A, 550, A122
Sitnova T. M., Yakovleva S. A., Belyaev A. K., Mashonkina L. I., 2022, MNRAS, 515, 1510
Skrutskie M. F. et al., 2006, AJ, 131, 1163
Sneden C., Cowan J. J., Gallino R., 2008, ARA&A, 46, 241
Starkenburg E. et al., 2017, MNRAS, 471, 2587
Suda T. et al., 2008, PASJ, 60, 1159
Tonry J. L. et al., 2012, ApJ, 750, 99
Tsymbal V., Ryabchikova T., Sitnova T., 2019, in Kudryavtsev D. O., Romanyuk I. I., Yakunin I. A., eds, ASP Conf. Ser. Vol. 518. Astron. Soc. Pac., San Francisco, p. 247
Tumlinson J., 2010, ApJ, 708, 1398

Van der Swaelmen M., Barbuy B., Hill V., Zoccali M., Minniti D., Ortolani S., Gómez A., 2016, A&A, 586, A1
Ventura P. et al., 2021, A&A, 655, A6

SUPPORTING INFORMATION

Supplementary data are available at *MNRAS* online.

Table 2. Line atomic data, LTE, and NLTE abundances, $\log \varepsilon$, for individual lines in Pr184237.

Please note: Oxford University Press is not responsible for the content or functionality of any supporting materials supplied by the authors. Any queries (other than missing material) should be directed to the corresponding author for the article.

This paper has been typeset from a TEX/LATEX file prepared by the author.